JCTC Journal of Chemical Theory and Computation

pubs.acs.org/JCTC Article

Nonadiabatic Dynamics in Si and CdSe Nanoclusters: Many-Body vs Single-Particle Treatment of Excited States

Brendan Smith,[§] Mohammad Shakiba,[§] and Alexey V. Akimov*

Cite This: *J. Chem. Theory Comput.* 2021, 17, 678−693 Read Online

ACCESS | Metrics & More | Article Recommendations | SI Supporting Information

ABSTRACT: In this work, we report a new nonadiabatic molecular dynamics methodology that incorporates many-body (MB) effects in the treatment of electronic excited states in extended atomistic systems via linear-response time-dependent density functional theory (TD-DFT). The nonradiative dynamics of excited states in $Si_{75}H_{64}$ and $Cd_{33}Se_{33}$ nanocrystals is studied at the MB (TD-DFT) and single-particle (SP) levels to reveal the role of MB effects. We find that a MB description of the excited states qualitatively changes the structure of coupling between the excited states, leading to larger nonadiabatic couplings and accelerating the dynamics by a factor of 2−4. The dependence of excited state dynamics in these systems on the surface hopping/decoherence methodology and the choice of the dynamical basis is investigated and analyzed. We demonstrated that the use of special "electron-only" or "hole-only" excitation bases may be advantageous over using the full "electron−hole" basis of SP states, making the computed dynamics more consistent with the one obtained at the MB level.

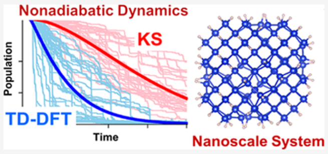

1. INTRODUCTION

Nonadiabatic dynamics (NAD) is a powerful tool for predicting the coupled evolution of electrons and nuclei. It can be used to detail excited state processes in chemical systems, such as hot carrier cooling,[1−8] electron−hole recombination,[9−19] and carrier−carrier and carrier−phonon scattering.[20] Multiple trajectory surface hopping (TSH) approaches are available nowadays for modeling NAD,[21−28] with methods like Tully's fewest switches surface hopping (FSSH) algorithm[29] being among the most adopted ones. Despite the simplicity of the TSH approaches, their application to modeling NAD in nanoscale systems and periodic solids is still prohibitively expensive. To enable such simulations, two key approximations are widely used: (a) the Neglect-of-Back-Reaction Approximation (NBRA) of Craig, Duncan, and Prezhdo,[30−32] which neglects the response of nuclear evolution to the change of electronic states upon photoexcitation or excited state decay; (b) the single-particle (SP) approximation in modeling electronic excited states, where the state energies and nonadiabatic couplings (NACs) are computed using the properties of 1-electron molecular orbitals (MOs) such as Kohn−Sham (KS) orbitals,[11,13,33−44] semiempirical or ab initio MOs,[33,45−52] and individual excited Slater determinants (SDs) built out of these types of SP orbitals.[34,53]

Although both the NBRA and SP description of excited states in nanoscale and condensed-matter systems have been widely used, their validity is mainly justified by an agreement with experiments, which can come due to favorable and uncontrollable error cancellation. Thus, it is important to further explore the validity of such critical approximations. The approach we undertake in this work is to use the approaches of higher conceptual rigor and conduct a comparative analysis with the cruder approximations to learn the qualitative effects of the better approximations. Whereas the validation of the NBRA could require its own attention, its validity is arguably easier to justify for large systems where the system's excited state reorganization energies could be comparable to thermal energies and hence the nuclear dynamics perturbation induced by electronic excitations could be comparable to that induced by available thermal fluctuations. On the other hand, the validity of the SP approach is far less trivial to justify in such extended systems.

As a rule of thumb, the excited states of small molecules are nearly always multiconfigurational, even for low excited states,[54,55] so the SP description would be inadequate most of the time. Many-body (MB) effects are expected to play a role in quantum-confined systems such as quantum dots and low-dimensional systems, or at low temperatures where exciton binding energies are comparable or larger than thermal energy. Indeed, a number of computational studies illustrated that the excited states of quantum dots[56,57] and perovskite solids[58,59] possess a strong multiconfigurational character. As such, it is of paramount importance to account for MB effects in NAD simulations of nanoscale systems and periodic solids and assess their effect on the computed transient dynamics.

To date, MB effects in NAD simulations of small molecules can be accounted for in a variety of packages[60,61] and at a variety of levels of theory. For periodic solids and nanoscale

Received: October 31, 2020
Published: January 15, 2021

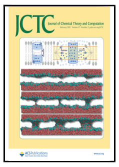

ACS Publications

systems, many-body perturbation theory (MBPT) is perhaps the most rigorous approach available today to describe optical properties and characterize excitons.[62−67] However, its excessive computational costs make it impractical to dynamical problems, where thousands of such calculations are needed. Some authors have utilized the many-body Bethe−Salpeter equation (BSE) formalism to correct the energy levels used in NAD calculations,[36] but no corrections to NACs have been reported at such a level.

As a cheaper alternative to approximately account for many-body effects, time-dependent density functional theory (TD-DFT) has been used to handle relatively large systems.[68] The time-dependent density functional tight binding (TD-DFTB) methodology[69] available through the DFTB+,[70,71] DFTBaby,[72] FIREBALL,[73] or Newton-X[60] packages and the collective electron oscillator (CEO) approach,[74−76] available through the NEXMD[51,52] package, have demonstrated their ability to handle NAD in large organic molecules up to several hundreds of atoms. Our present interest lies in the domain of periodic solids and nanoscale clusters, where the NAD is still limited to the SP formalism, such as KS-DFT.[10,13,34,35,45,77−86] Thus, the use of TD-DFT in the context of the NAD in nanoscale clusters and periodic systems is the most viable scheme to account for MB effects in such extended systems.

In this work, we report the development of a new computational methodology to conduct the NBRA-TSH calculations of NAD in nanoscale systems that also accounts for MB effects. This computational workflow is implemented as part of the open-source Libra[87] package for NAD. It is designed to be a general module that can be interfaced with a variety of electronic structure calculation packages, although in this work, we utilize the CP2K software package[88,89] as the driver for the underlying TD-DFT calculations. The present computational framework allows us to compute NACs and state energies both at the SP (KS-DFT) and MB (TD-DFT) levels. The utility of the resulting computational methodology is demonstrated by studying the role of MB effects in the NAD of Si and CdSe nanocrystals (NCs). We compare the NAD in the two systems computed using NACs and energies obtained at the SP and MB levels and analyze the induced differences in the excited state dynamics. We also discuss the role of the dynamical basis choice and decoherence scheme.

2. THEORY AND METHODS

2.1. Nonadiabatic Dynamics Methodology.

The overall time-dependent wavefunction of the system is represented as

$$X(\boldsymbol{r}; t) = \sum_{I=0}^{N-1} c_I(t)\Psi_I(\boldsymbol{r}; \boldsymbol{R}(t)) \tag{1}$$

Here, $\{\Psi_I\}$ is a vector of all electronic states involved in the dynamics, which we refer to as the *dynamical basis*, $\{c_I(t)\}$ is a vector of the corresponding time-dependent amplitudes, and N is the number of dynamical basis functions used. The evolution of the overall wavefunction, eq 1, follows the time-dependent Schrodinger equation (TD-SE):

$$i\hbar\frac{\partial X}{\partial t} = \hat{H}X \tag{2}$$

Here, $\hat{H} = \hat{T}_R + \hat{H}_{el}$ is the system's Hamiltonian, with the components $\hat{T}_R$ and $\hat{H}_{el}$ being the nuclear kinetic energy and electronic Hamiltonian operators, respectively. Within the classical path approximation (CPA),[29,90] the electronic Hamiltonian is assumed to be functionally dependent on electronic coordinates, $\boldsymbol{r}$, and only parametrically dependent on nuclear coordinates, which may change with time, $\boldsymbol{R} = \boldsymbol{R}(t)$: $\hat{H}_{el} = \hat{H}_{el}(\boldsymbol{r}; \boldsymbol{R}(t))$. The dynamical basis states, $\{\Psi_i\}$, are chosen as the eigenstates of the electronic Hamiltonian, $\hat{H}_{el}(\boldsymbol{r}; \boldsymbol{R}(t))$, and therefore are also parameterized by nuclear trajectories:

$$\hat{H}_{el}(\boldsymbol{r}; \boldsymbol{R}(t))\Psi_I(\boldsymbol{r}; \boldsymbol{R}(t)) = E_I(\boldsymbol{R})\Psi_I(\boldsymbol{r}; \boldsymbol{R}(t)) \tag{3}$$

Some algebra yields the equations of motion for the dynamical basis amplitudes, $\{c_I(t)\}$, which play the role of the effective electronic degrees of freedom (DOFs):

$$i\hbar\frac{\partial c_I(t)}{\partial t} = \sum_J [E_J(t)\delta_{I,J} - i\hbar D_{I,J}(t)]c_J(t). \tag{4}$$

Here, $E_J(t) = E_J(\boldsymbol{R}(t))$ and $D_{I,J}(t) = D_{I,J}(\boldsymbol{R}(t)) = \langle\Psi_I|\frac{\partial}{\partial t}\Psi_J\rangle$ are the adiabatic energy of electronic state J and the NAC for the pair of states I and J, respectively. These properties are our main interest in this work.

Following the NBRA framework adopted here, nuclear trajectories are obtained by solving the classical Newtonian equations of motion for nuclei with forces determined quantum-mechanically for a single potential energy surface, which is typically taken to be the ground potential energy surface:

$$M_\alpha\ddot{\boldsymbol{R}}_\alpha(t) = -\frac{\partial E_0(\boldsymbol{R})}{\partial \boldsymbol{R}_\alpha} \tag{5}$$

where M_α is the mass of the nuclear DOF α.

The time-integration of eqs 4 and 5 provides the input to perform TSH calculations within the NBRA as well as to compute state tracking, decoherence, and phase corrections. In particular, our implementation includes the NBRA adaptations of the FSSH,[29] Markov state surface hopping (MSSH),[91] global flux surface hopping (GFSH),[92] surface hop proposal algorithms, and a variety of hop acceptance algorithms as detailed elsewhere.[93] Decoherence algorithms such as decoherence-induced surface hopping (DISH),[94] modified simple decay of mixing (mSDM),[93,95] and instantaneous decoherence at the attempted hops (ID-A)[96] are also available. These schemes are also reviewed in our previous work.[93] The integration of the TD-SE, eq 4, is conducted using a norm-conserving geometric integrator described in an earlier work.[78]

2.2. Dynamical Basis and Overlaps.

In our formulation, the dynamical basis is chosen as a linear combination of SDs, $\Phi_{J = [j_0, j_1, \ldots, j_{K-1}]}$, enumerated by the composite indices like $J = [j_0, j_1, \ldots, j_{K-1}]$:

$$\Psi_I(t) = \sum_{J=0}^{M-1} t_{I,J}(t)\Phi_{J=[j_0,j_1,\ldots,j_{K-1}]} \tag{6}$$

Here, $\Phi_{J = [j_0, j_1, \ldots, j_{K-1}]}$ are the SDs:

$$\Phi_{J=[j_0,j_1,\ldots,j_{K-1}]} = \frac{1}{\sqrt{K!}}\det|\psi_{j_0}, \psi_{j_1}, \cdots, \psi_{j_{K-1}}| = \frac{1}{\sqrt{K!}}\det\begin{vmatrix} \psi_{j_0}(0, t) & \ldots & \psi_{j_0}(K-1, t) \\ \vdots & \ddots & \vdots \\ \psi_{j_{K-1}}(0, t) & \ldots & \psi_{j_{K-1}}(K-1, t) \end{vmatrix} , \tag{7}$$

which are constructed of K 1-particle spin-orbitals, $\psi_{j_k}(t) = \phi_{j_k}(t)\sigma_{jk}$, $\sigma_{j_k} \in [\alpha, \beta]$, $k = 0, \cdots, K-1$. The number K is selected as the number of all distinct 1-particle orbitals needed to construct all SDs that appear in all dynamical basis functions. In other words, this number may depend on the numbers N and M that appear in eqs 1 and 6, respectively. The underlying spatial and spin functions obey the following relationships:

$$\langle\phi_{i_k}(t)|\phi_{j_l}(t')\rangle = \begin{cases} \delta_{i_k,j_l}, & t = t' \\ s_{i_k,j_l}, & t \neq t' \end{cases}, \quad \langle\sigma_{i_k}|\sigma_{j_l}\rangle = \delta_{i_k,j_l} \tag{8}$$

Here, $s_{i_k,j_l} = \langle\phi_{i_k}(t)|\phi_{j_l}(t')\rangle$ is the overlap of the spatial components of molecular orbitals but taken at different geometries (as parameterized by the time variable, t), $\phi_{i_k}(t)$ and $\phi_{j_l}(t')$, where $k, l = 0, \cdots, K-1$. The overlaps of the kind eq 8 give the elements of the transition density matrix (TDM), which is also commonly referred to as the time-overlap matrix. The TDM is the central property in our calculations, since it can be used to compute the NACs, and is needed to compute phase consistency corrections, and to track states' identity evolution at trivial crossings.

Note that the ansatz eq 6 is suitable for representing both the MB/excitonic (configuration interaction/TD-DFT) and the SP wavefunction. In the latter case, each dynamical basis function would be taken as a single excited SD. This would be the case used previously in multiple studies and the one that we want to evaluate in comparison to the case using the more accurate excitonic wavefunctions (given by TD-DFT). It is worth explaining the terminology. Although the single excited SDs are functions of multiple electrons, the NACs computed with such functions can be reduced to the couplings between individual 1-electron functions (orbitals). Thus, these functions are still regarded as single-particle states, whereas the superpositions of the type eq 6 are referred to as the MB states.

NACs in the dynamical basis, $D_{I,J}(\boldsymbol{R}(t)) = \langle\Psi_I|\frac{\partial}{\partial t}\Psi_J\rangle$, are computed numerically via the Hammes−Schiffer−Tully (HST) approach:[97]

$$\begin{aligned} D_{I,J}\left(t + \frac{\mathrm{dt}}{2}\right) &\approx \frac{\langle\Psi_I(t)|\Psi_J(t + \mathrm{dt})\rangle - \langle\Psi_I(t + dt)|\Psi_J(t)\rangle}{2\mathrm{dt}} \\ &= \frac{S_{I,J}(t, t + \Delta t) - S^{*}_{J,I}(t, t + \Delta t)}{2\Delta t} \end{aligned} \tag{9}$$

The time overlaps, $S_{I,J}(t, t + \Delta t) = \langle\Psi_I(t)|\Psi_J(t + \Delta t)\rangle$, are computed via a linear transformation of the time overlaps in the SD basis:

$$\begin{aligned} &\langle\Psi_I(t)|\Psi_J(t + \Delta t)\rangle \\ &\quad = T^{+}(t)\langle\Phi_{I=[i_0,i_1,..,i_{K-1}]}(t)|\Phi_{J=[j_0,j_1,..,j_{K-1}]}(t + \Delta t)\rangle \\ &\qquad T(t + \Delta t) \end{aligned} \tag{10}$$

Here, the matrix T contains the TD-DFT amplitudes of all excited states, as they appear in eq 6:

$$T(t) = \begin{pmatrix} t_{0,0}(t) & \dots & t_{0,N-1}(t) \\ \vdots & \ddots & \vdots \\ t_{M-1,0}(t) & \dots & t_{M-1,N-1}(t) \end{pmatrix} \tag{11}$$

Here, M is the size of the SD basis used to represent the excited states, eq 6. In practice, the TD-DFT wavefunctions can be expressed using a large number of SDs. However, we allow users to discard terms whose amplitudes are below a specified threshold. This filtering approach leads to a significant reduction of M values and hence to faster computations. The number N indicates the size of the dynamical basis used in eq 1 and is controlled by the user. The selection of this number is based on the physical chemistry of the problems—knowing which states are relevant to the studied problem. The CI coefficients remaining after the abovementioned truncation are renormalized before they are used in the calculations of NACs in eq 9. It is worth mentioning that the truncation should account for the time evolution of the CI coefficients. One may encounter occurrences of the CI coefficients being smaller than the specified threshold at one point of the trajectory and above it at another point. In such cases, underlying SD basis functions are included in the dynamics, so the corresponding terms are not truncated. An analysis of the CI coefficients is first run along the precomputed trajectories to determine the basis of the SD states to be used in the truncation.

The overlap matrix of the SDs is calculated as follows:[98,99]

$$\begin{aligned} S_{I,J}(t, t') &= \langle\Phi_{I=[i_0,i_1,..,i_{K-1}]}(t)|\Phi_{J=[j_0,j_1,..,j_{K-1}]}(t')\rangle \\ &= \det\begin{vmatrix} s_{i_0,j_0}(t, t')\langle\sigma_{i_0}|\sigma_{j_0}\rangle & \dots & s_{i_0 j_{K-1}}(t, t')\langle\sigma_{i_0}|\sigma_{j_{K-1}}\rangle \\ \vdots & \ddots & \vdots \\ s_{i_{K-1},j_0}(t, t')\langle\sigma_{i_{K-1}}|\sigma_{j_0}\rangle & \dots & s_{i_{K-1} j_{K-1}}(t, t')\langle\sigma_{i_{K-1}}|\sigma_{j_{K-1}}\rangle \end{vmatrix} \end{aligned} \tag{12}$$

To compute the time overlaps of molecular orbitals, we use a numerical integration of the "Gaussian cube"[100] files, which is a standard and widely used format for representing the wavefunctions numerically. The details of our implementation are discussed in Section 1 of the Supporting Information. Although an approach based on the processing of large files such as these could be viewed to be disadvantageous, it allows for facile switching between different software packages because the files of this format can be produced by most of electronic structure codes. In addition, this format is independent of the way the wavefunctions are represented internally—whether numerically, in a localized atomic basis, delocalized plane-wave basis, or any other mixed format. Thus, the approach adopted here can be readily extended to a variety of software packages.

Although some packages such as nano-qmflows[101] allow computing the time overlaps of molecular orbitals via transforming the analogous time overlaps of the atomic orbitals analytically, one would need to be careful and knowledgeable about the details of the atomic orbitals used. Considering the multitude of formats and variations of the atomic orbital bases, the approach would require some expertise to be used correctly. Moreover, nano-qmflows is not applicable to mixed bases, plane waves, or Slater-type orbitals, often used in semiempirical methods. In addition, some packages (e.g., DFTB+[71]) are known to have difficulties in computing the time overlaps of atomic orbitals when the displacements are too small, owing to the way in which the wavefunctions are constructed. The use of the numerical "cube" files can potentially mitigate such problems, and their use in NAD studies warrants attention.

2.3. State Energies.

The state energies, $E_J(t)$, entering eq 4 can be computed in one of the two following ways. In the SP treatment, the SDs are used as the dynamical basis. Following the earlier prescription,[34,78] we approximate the energies of such states by the sums of the occupied 1-electron orbital energies, ϵ_i:

$$E_{I=[i_0,i_1,..,i_{K-1}]} = \sum_{k=0}^{K-1} \epsilon_{i_k}. \tag{13}$$

A more rigorous computation of the energies of such SD states would require additional exchange and Coulomb integrals as well as an evaluation of the exchange-correlation functional for the excitations considered. In principle, such a calculation could be done using the ΔSCF methodology,[102] but in the present work, we do not consider it. One of the reasons is because the approach based on eq 13 relies on the readily available 1-electron properties and therefore has been widely adopted. Thus, the use of eq 13 is better suited for assessing the SP approximation used in the NAD of nanoscale and periodic systems. The computed excited state energies and NACs for all dynamical basis states are used to construct the vibronic Hamiltonians at every timestep of the trajectory. These data are stored on disk for further re-use in NAD calculations.

2.4. State Tracking.

State tracking is of great importance for NAD simulations to be reliable and reproducible. The problem of state tracking has long been recognized, and several prescriptions are available.[103−105] Following the earlier works of Fernandez-Alberti et al.,[103] we adapt the "min-cost" (also known as Munkres−Kuhn (MK) or "Hungarian") algorithm, available through the Libra package. Unlike on-the-fly implementations, such as the one used by Fernandez-Alberti, where the states' identity change affects the electron-nuclear dynamics, state tracking within the NBRA framework can be done simply by reorganizing the structure of the corresponding time-overlap matrices. Thus, instead of swapping the state indices and time-evolved amplitudes, we reorder elements of the time-overlap matrices to affect how electronic amplitudes evolve and how surface hops are proposed.

The state reordering algorithm used in this work is summarized in Scheme 1 and its workflow is further illustrated in Figures S1 and S2 of the Supporting Information. Here, we denote the dynamical basis functions that are available directly from the electronic structure calculations as the "raw" wavefunctions and label them $|\Psi\rangle = (\Psi_0, \Psi_1, \cdots, \Psi_{N-1})$. The properly ordered (referred to as the dynamically consistent) states are marked with the tilde, that is $|\tilde{\Psi}\rangle = (\tilde{\Psi}_0, \tilde{\Psi}_1, \cdots, \tilde{\Psi}_{N-1})$. The key idea of the state tracking algorithm is to compute a sequence of permutation matrices, $\{P(t_n)\}$, that can be used to recover the dynamically consistent states (and hence the properties) from the raw ones at any point in time. In this work, we use the convention that the permutation matrices reorder the "raw" states such that the reordered states at any given time t_n, $|\tilde{\Psi}(t_n)\rangle = |\Psi(t_n)\rangle P_n$,are consistent with the ordering of the states in the state vector at the previous timestep, $|\tilde{\Psi}(t_{n-1})\rangle$, with $|\tilde{\Psi}(t_0)\rangle = |\Psi(t_0)\rangle$. The consistency of the ordering is quantified by the cost matrices defined as $C_{ij}(n) = |S'_{ij}(t_n, t_{n+1})|^2$, where $S'_{ij}(t_n, t_{n+1}) = \langle\tilde{\Psi}_i(t_n)|\Psi_j(t_{n+1})\rangle$ is the modified time-overlap matrix. Note that the elements of the cost matrix do not depend on the phases of the wavefunctions and that the variable used to denote the cost matrix, C, should not be confused with the variable, c, used in eqs 1 and 4. Thus, the potential phase-inconsistency problem does not affect this step. This also means that phase corrections should be performed after the state reordering.

Scheme 1. Generic Idea of the State Reordering Algorithm Used in This Work

```
1) $t = t_0$, $P_0 = I$
2) For the rest of steps ($n = 1, \ldots N_{steps} - 1$) or until converged, repeat the following:
    a. Compute: $S'(t_n, t_{n+1}) = P_n^+ S(t_n, t_{n+1})$ by simply permuting the rows of
       $S(t_n, t_{n+1})$ according to $P_n$;
    b. Compute the cost matrix: $C_{ij}(t_n, t_{n+1}) = |S'_{ij}(t_n, t_{n+1})|^2$;
    c. Solve the optimal assignment problem (maximize) using the cost matrix and
       Munkres-Kuhn algorithm: $P_{n+1} = MK(C(t_n, t_{n+1}))$;
    d. Compute: $S''(t_n, t_{n+1}) = S'(t_n, t_{n+1}) P_{n+1}$ by simply permuting the columns
       of $S'(t_n, t_{n+1})$ according to $P_{n+1}$;
3) Set $n = n + 1$;  Go to step 2
```

Finally, once the instantaneous state permutation matrices are found, they can be used to transform the "raw" time overlaps of the wavefunctions at adjacent time steps, $S(t_n, t_{n+1}) \equiv \langle\Psi(t_n) | \Psi(t_{n+1})\rangle$, into those between the dynamically consistent states, $S''(t_n, t_{n+1}) \equiv \langle\tilde{\Psi}(t_n)|\tilde{\Psi}(t_{n+1})\rangle$. The latter are used to compute the phase corrections as discussed in the next section, and eventually to compute the NACs as described in Section 2.2. Furthermore, the time-local permutation matrices are used to compute the cumulative permutation matrices that can be used to find out the reordering of the current "raw" states relative to the original ordering states at the beginning of the simulation. Further details regarding the state tracking algorithm, the underlying theory and implementation, and the used conventions and relationships are presented in Section 2 of the Supporting Information.

The state tracking algorithm is applied at the level of dynamical basis functions, which are chosen as either the individual SDs (for the SP description) or as the TD-DFT excited states given as superpositions of SDs, eq 6. All the underlying levels of wavefunctions are considered auxiliary, so there is no physical meaning in tracking their identities.

As alluded to above, in the context of NBRA calculations, state tracking is equivalent to reordering of the matrix elements of the time-overlap matrices, so we also refer to this step as the state reordering. We clarify that the reordering applies only to the time-overlaps since they reflect the intrinsic state identities. The original ordering of the states' energies obtained from electronic structure calculations (usually according to the Aufbau principle) is not changed by our reordering procedure.

2.5. Phase Consistency Correction.

Once the states have been reordered according to their natural identities, the phase consistency correction[106] is applied. Analogous to state tracking, the phase correction is applied at the level of the dynamical basis functions. Within the NBRA, it simply means changing the underlying time-overlap matrices (after the state reordering is applied). Following a recipe described earlier,[106] the phase correction is defined by

$$F_i(t_{n+1}) = \frac{\langle \tilde{\Psi}_i(t_n) | \Psi_i(t_{n+1}) \rangle}{\| \tilde{\Psi}_i(t_n) \| * \| \Psi_i(t_{n+1}) \|} = \frac{\langle \tilde{\Psi}_i(t_n) | \Psi_i(t_{n+1}) \rangle}{\| \Psi_i(t_n) \| * \| \Psi_i(t_{n+1}) \|} \tag{14}$$

such that the phase corrected wavefunction at t_{n+1} is given by

$$\tilde{\Psi}_i(t_{n+1}) = \Psi_i(t_{n+1}) F_i^*(t_{n+1}) \tag{15a}$$

In matrix notation

$$| \tilde{\Psi}(t_{n+1}) \rangle = | \tilde{\Psi}(t_{n+1}) \rangle F^*(t_{n+1}) \tag{15b}$$

Here, the tilde notation is used to denote the phase-corrected wavefunctions and those without tilde denote the "raw", uncorrected wavefunctions, but those with the state-reordering applied to them. In this regard, the tilde used here should not be confused with the tilde used in Section 2.4. Here, $F_{n+1} = F(t_{n+1}) = \text{diag}\,\{F_i(t_{n+1})\}$ is a diagonal matrix composed of the phase correction factors, eq 14, for all states, $i = 0, \cdots, N - 1$. The F matrices defined above contain the cumulative phase correction factors gained along the given trajectory. In practice, it is convenient to work with the instantaneous phase correction factors, which can be computed from the "raw" time-overlaps (state-tracking-corrected):

$$\begin{aligned} f_i(t_{n+1}) &\equiv \frac{\langle \Psi_i(t_n) | \Psi_i(t_{n+1}) \rangle}{\| \Psi_i(t_n) \| * \| \Psi_i(t_{n+1}) \|} \\ &= \frac{S_{ii}(t_n, t_{n+1})}{\sqrt{S_{ii}(t_n, t_n)}\,\sqrt{S_{ii}(t_{n+1}, t_{n+1})}} \end{aligned} \tag{16}$$

Analogous to the matrix representation of F_n, it is convenient to introduce the matrix of instantaneous phase correction factors: $f_{n+1} = f(t_{n+1}) = \text{diag}\,\{f_i(t_{n+1})\}$. Comparing eqs 14 and 16 and considering the transformation eq 15, we can relate the cumulative and instantaneous phase correction factors (in matrix representation) as

$$F_n = \prod_{k=0}^{n} f_k \tag{17}$$

$$F_{n+1} = f_{n+1} F_n \tag{18}$$

In practical implementation, we are interested in correcting the time-overlap matrix, $S(t_n, t_{n+1})$, and not necessarily the wavefunctions themselves. The time-overlap matrix with the phase-corrected states can be computed as

$$\begin{aligned} S''(t_n, t_{n+1}) &\equiv \langle \tilde{\Psi}(t_n) | \tilde{\Psi}(t_{n+1}) \rangle = F_n \langle \Psi(t_n) | \Psi(t_{n+1}) \rangle F_{n+1}^* \\ &= F_n S(t_n, t_{n+1}) F_{n+1}^* \end{aligned} \tag{19}$$

Note that although the transformations in eq 19 are written in the matrix form, transformations involving the diagonal matrices use element-wise multiplications in practice for efficiency. A pictorial summary of the algorithm is presented in Figure S3 of the Supporting Information.

2.6. Systems, Computational Details, and Analysis Procedures. The developed methodology is applied to study the role of MB effects in the NAD of a low-symmetry (C_1) silicon nanocrystal (NC), $Si_{75}H_{64}$[107] and the $Cd_{33}Se_{33}$ magic-cluster, which is one of the smallest stable CdSe clusters detected experimentally.[108] In the following sections, we refer to these systems as the Si NC and CdSe NC, respectively. The geometry optimization, TD-DFT, and AIMD for the NCs are performed using the CP2K software package.[88,89] Relevant computational details are summarized in Section 4 of the Supporting Information.

For the NAD, the initial excited states are selected to be approximately 0.7 eV above the first excited state for the Si NC and approximately 0.7 to 0.8 eV above the first excited state for the CdSe NC (the 1P excitation[109]). For the MB and SP bases, the initial states are chosen as the excited states whose energies are within the indicated energy regions. This leads to four states being selected for each type of calculation. For the hole- and electron-only bases, three electronic excited states are considered. These excitation energies are chosen in accordance with the reported experiments.[110−113] We considered eight geometries along the precomputed nuclear trajectories as starting points for the NAD, where each considered geometry is separated by 200 fs of nuclear evolution. For each NAD simulation, 250 realizations of the stochastic TSH trajectories are used. Thus, for each type of calculation, the properties of interest (e.g., populations or energies) are computed based on averaging or statistical analysis of the overall 2000 trajectories. As for the TSH algorithms, we consider the FSSH, and two decoherence schemes: ID-A and mSDM.

The NAD is quantified by fitting a stretched-compressed exponential function to 1.0 minus the recovery of the electronic excited states to which the initial electronic excitation transitions to

$$P(t; E_0) = \exp\left(-\left(\frac{t}{\tau}\right)^{\beta}\right) \tag{20}$$

where β is a fitting parameter that describes the kinetics of the transition and τ is a fitting parameter to describe the lifetimes of the dynamics. Equation 20 is used for each of the initial conditions selected for a given system as described above. Only the fits that have the R^2 factor larger than 0.8 are utilized to compute the average timescales and the uncertainties/error bars. The error bars of the reported τ and β parameters are computed as

$$\varepsilon = Z \frac{s}{\sqrt{N}}. \tag{21}$$

where Z is the confidence interval coefficient, s is the standard deviation of data, and N is the number of samples (successful fits, whose R^2 values exceed 0.8). Here, we use a Z value of 1.96, which is representative of a confidence interval of 95% for the error bars.

3. RESULTS AND DISCUSSION

3.1. Electronic Structure at the Single-Particle Level.

The partial density of states computed for the optimized geometries of the two systems at the PBE level shows sizable band gaps (Figure 1) of 1.22 and 1.92 eV for CdSe and Si NCs, respectively. The occupied orbitals (hole states) of the Si NC have a dominant Si p character, whereas the unoccupied orbitals (electron states) are represented by a mix of Si p and d electrons. In CdSe, the hole states are represented by Se p orbitals and the electron excitation states mix Cd s, p, and d orbitals and a notable fraction of Se p orbitals.

The band gap of the Si NC is underestimated with respect to the experimental[114] band gap of roughly 2.7 eV for amorphous quantum dots of a slightly smaller size and is much smaller than the 3.4 eV band gap of a crystalline silicon quantum dot. Mavros et al.[115] have shown that nanocrystal symmetry is a key descriptor between crystalline and amorphous hydrogen

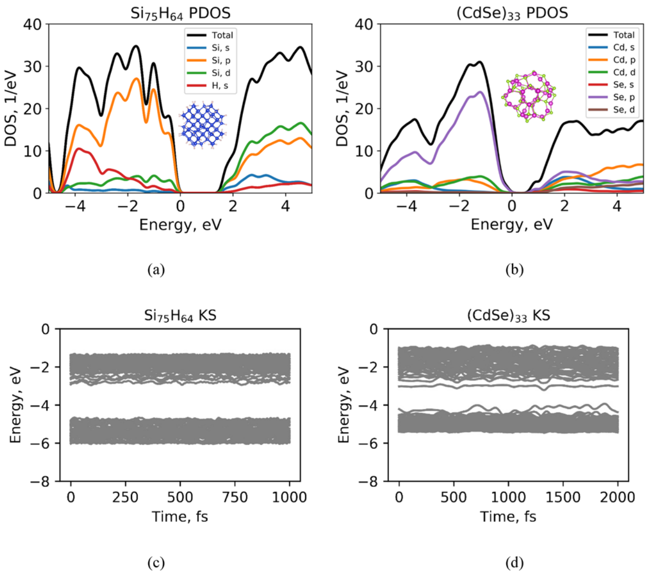

Figure 1. Orbital-resolved partial density of states (pDOS) for the (a) Si and (b) CdSe NCs. Time evolution of the KS energy levels for the (c) Si and (d) CdSe NCs.

terminated silicon quantum dots. Nanocrystals can be classified as being crystalline if their structure belongs to symmetry point groups higher than C_1, whereas amorphous Si NC have explicit C_1 point group symmetry. As such, it is appropriate to consider the Si NC used in this work of explicit C_1 point group symmetry to be amorphous. The band gap of the CdSe NC (1.22 eV) is in agreement with the one computed at the PBE level (1.44 eV) by Bokareva et al.,[116] although it is significantly underestimated compared to the one obtained by the same team using the optimally tuned range-separated hybrid functional (4.04 eV). Kilina et al.[117] reported band gaps ranging from 2.48 eV at the Hartree−Fock level to 2.80 eV at the B3LYP/LANL2DZ level for the same stoichiometry of CdSe NC as used in our present work.

The computed band gaps are on the smaller side in comparison to other reported results,[114−117] which stems from the well-known deficiency of pure density functionals such as the PBE[118] functional used in this work. Although this problem could be resolved by employing range-separated hybrid functionals, such calculations would be out of our computational power reach, especially as far as the TD-DFT calculations are concerned. Importantly, the NAD calculations reported in this work focus on the dynamics of excited states excluding electron−hole recombination.

The KS orbitals form very dense manifolds of occupied and unoccupied states (Figure 1c,d). The density of the occupied orbitals (holes states) is higher than that of the unoccupied states (electronic excitations) in both systems. Consequently, we expect that the dynamics of holes (or hole-dominated dynamics of MB excited states) would be faster than that of electrons (or electron-dominated excited states). By construction, the KS states are adiabatic and show no trivial crossings, although the orbitals can get degenerate or nearly degenerate many times during the dynamics.

3.2. Electronic Structure at the Many-Body Level. The composition of the TD-DFT excited states is quantified by the squares of the configuration interaction (CI) coefficients with which certain excited SD mix in the TD-DFT wavefunctions (Figure 2). We observe that a single SD excitation dominates

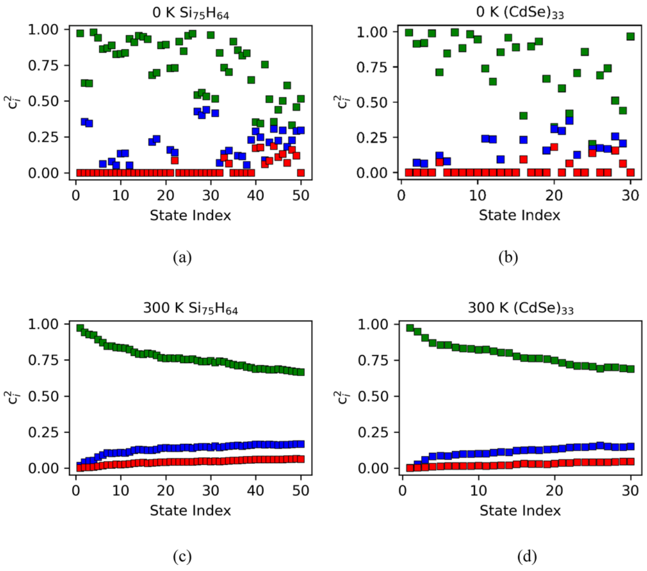

Figure 2. Squares of three largest CI coefficients for each of the excited states computed for the Si (a, c) and CdSe (b, d) NCs at their optimized geometries (a, b) and their average values obtained from the MD at 300 K (c, d).

the composition of the lowest excited states in both systems. Thus, the SP approximation is justified to model the excited states dynamics at lower excitation energies in these systems, including electron−hole recombination,[119] provided the band gap is corrected. This is also consistent with the general expectation of the applicability of the SP picture to such processes.[120] The SP approximation gradually breaks down for higher excited states, as the weights of the three leading SP excitations become comparable to each other. The TD-DFT calculations show that the excited state composition is sensitive to structural changes in both systems. The snapshots for the optimized geometry (Figure 2a,b) show a notable fraction of multiple SDs for low excited states. A thermal averaging over many such MD snapshots makes the dependencies smoother (Figure 2c,d) in comparison to the snapshot for the optimized geometry. The averaged curves follow the scattered area outlined by the optimized calculation (Figure 2a,b), suggesting that the excited states may mix in different excited SDs at different times, depending on the geometry. The comparisons of the two cases also suggest that the mixing of the SD excitations at the TD-DFT level at any instant may be stronger than the averaged plots suggest.

The NACs in the SP picture display a scattered appearance (Figure 3a,b), unlike in many reported time-domain simulations,[6,79,121−125] where the maximal values of time-averaged NAC magnitudes appear along the diagonal of such map plots. We attribute such a structure of the NAC matrices to the nature of the SD states after they are ordered according to their energies. In the SP picture, only those SDs that differ by a single electron excitation are coupled to each other. In a series of excitations, HOMO-N → LUMO+M, with either N or M fixed, the nearby energy states differ from each other by 1 electron excitation and are coupled to each other. The coupling decreases with either N (for fixed M, hole-only excitations) or M (for fixed N, electron-only excitations) increasing, leading to the “diagonal”-looking NAC maps with the NAC magnitudes decreasing as one moves away from the main diagonal (Supporting Information, Figure S4). In

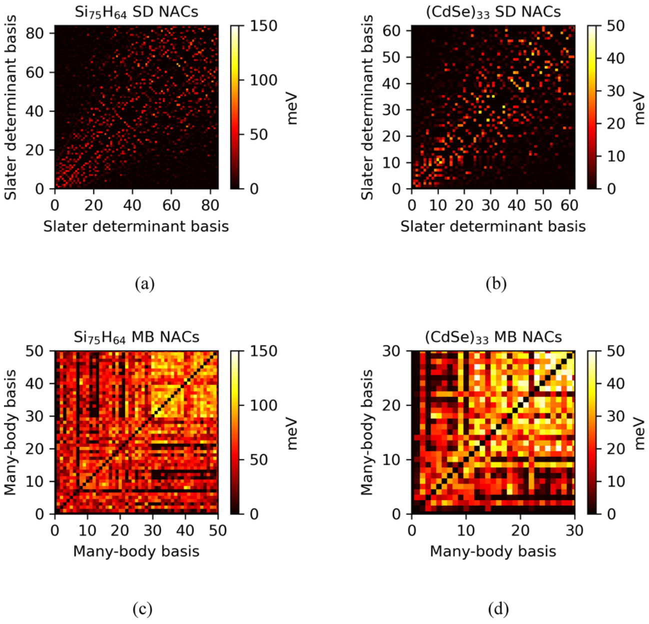

Figure 3. Time-averaged NAC magnitudes for the Si (a, c) and CdSe (b, d) NC systems in the SP (a, b) and MB (c, d) bases.

excitations with a simultaneous variation of *N* and *M* values, the nearby energy states may differ by more than 1 electron excitation (hence zero NACs) or by distant (weakly interacting) 1-electron orbitals, leading to small couplings. As a result, the NAC maps appear scattered in the SP-based basis of all possible electron−hole excitations (Figure 3a,b). This special structure of the NAC map can be regarded as a manifestation of the diabatic nature of the SD states constructed as mixed electron−hole excitations. At this level of description of their energies, such states do not have mutual "repulsion" (interaction) and thus are prone to the trivial crossing, leading to the scattered structure of the NAC matrices.

On the contrary, the MB states (given by TD-DFT in this work) have mutual interaction already encoded into them. Naturally, the MB states are all well coupled with many other MB states, across a wide range of energies (Figure 3c,d). Such pronounced couplings originate from the multideterminantal nature of the wavefunctions: composed of multiple SDs, the MB states may become coupled with the strongly coupled SD states present in each of them. As a result, the voids in the scatter-like appearance of the NAC matrix in the SP basis are filled in the MB basis. The use of the dynamical basis functions taken as SDs with the electron-only or hole-only excitations leads to the expected diagonal-like structure of the NAC matrix (Supporting Information, Figure S4), which was observed in numerous past NAD studies that utilized exactly such bases,[20,35,40,125−130] although the use of the extensive bases of mixed electron−hole excitations has been reported as well.[131−134] Our present analysis of the NAC matrices (and the following analysis of the dynamics) suggests that although the former modeling approaches can be justified, the latter might need further re-evaluation since they might be missing the critical interactions of the used "diabatic" states with each other, although some works addressed this problem by introducing empirical corrections to the computed energies.[134]

Finally, it is instructive to compare the NAC magnitudes for the two systems and for the two types of the electronic structure treatments. Such comparisons are not straightforward based only on Figure 3. Thus, we compute the probability density distribution of NAC magnitudes for all pairs of states as sampled by our adiabatic trajectories (Figure 4). First, the probability density of NACs is larger for the Si NCs, as what follows from the comparison of the probability densities of larger NACs (e.g., Figure 4b vs e; c vs f). We attribute this difference to the somewhat higher densities of KS states in the Si NC system as compared to that in CdSe NC (Figure 1). Thus, we can expect somewhat faster dynamics in Si NCs than in CdSe NCs. Second, we observe that the probability densities of the NACs computed at the MB level of theory are slightly shifted to larger NAC magnitudes in comparison to those computed at the SP level. This is true for both systems. Indeed, the probability densities for small NACs, less than ca. 1 meV, are higher at the SP level (Figure 4a,d). This is followed by a noticeable shoulder in the range of 1−3 meV in the MB (blue lines) treatment of electronic states. Going further, although the probability of encountering even larger NACs up to 125 meV decreases, the probabilities are notably larger if NACs are computed using MB states in contrast to those computed using the SP states (e.g. Figure 4c,f). Thus, we expect that the inclusion of the MB effects should accelerate the relaxation dynamics of excited states in both systems.

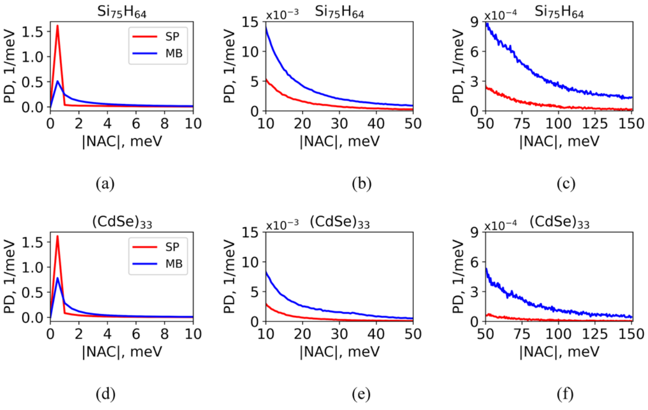

Figure 4. Probability density (PD) of NAC magnitudes for all pairs of states sampled over the MD trajectories of both systems: (a, b, c) Si NC; (d, e, f) CdSe NC. Columns show distributions for distinct ranges of NAC magnitudes for better visibility. Note that the PDs of the NAC magnitudes are slightly shifted toward larger values in the MB basis.

3.3. Nonadiabatic Dynamics.

To test the developed NAD methodology and tools and to assess the role of MB effects, we compute the decay dynamics of excited states chosen to be roughly 0.7−0.8 eV above the first excited state. Because of the high density of states at this energy range, the population of each individual state may oscillate for a long time due to coherences and strong coupling with nearby states. Such persistent oscillations may not give an adequate description of the overall process of the excited state energy relaxation in the considered systems. Thus, we study the recovery dynamics of the lower excited states, which is equivalent to the depopulation of all the initial "hot" excited states, rather than to the depopulation of a single initial state. Thus, the identity of the initially populated state is virtually irrelevant, with the only exception discussed below. The dynamics computed for Si and CdSe NCs with several TSH approaches is summarized in Figures 5 and 6, respectively. The

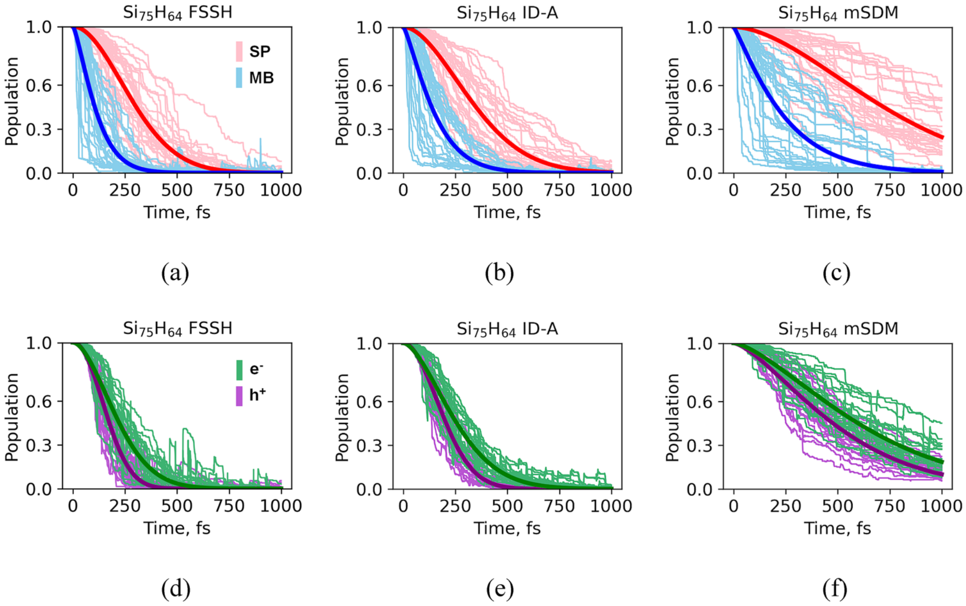

(a) (b) (c)

(d) (e) (f)

Figure 5. Decay of the total population of all "hot" excited states to the lowest two excited states in the Si NC in the SP and MB dynamical bases: SP with all electron−hole excitations (red lines, a−c), MB (blue lines, a−c), and SP with electron-only (green lines, d−f) or hole-only (purple lines, d−f) excitations. Various TSH approaches are used: FSSH (a, d), ID-A (b, e), and mSDM (c, f). The average population for each case is shown in bold lines, whereas thin lines illustrate the population dynamics for each initial condition (excited state and nuclear trajectory).

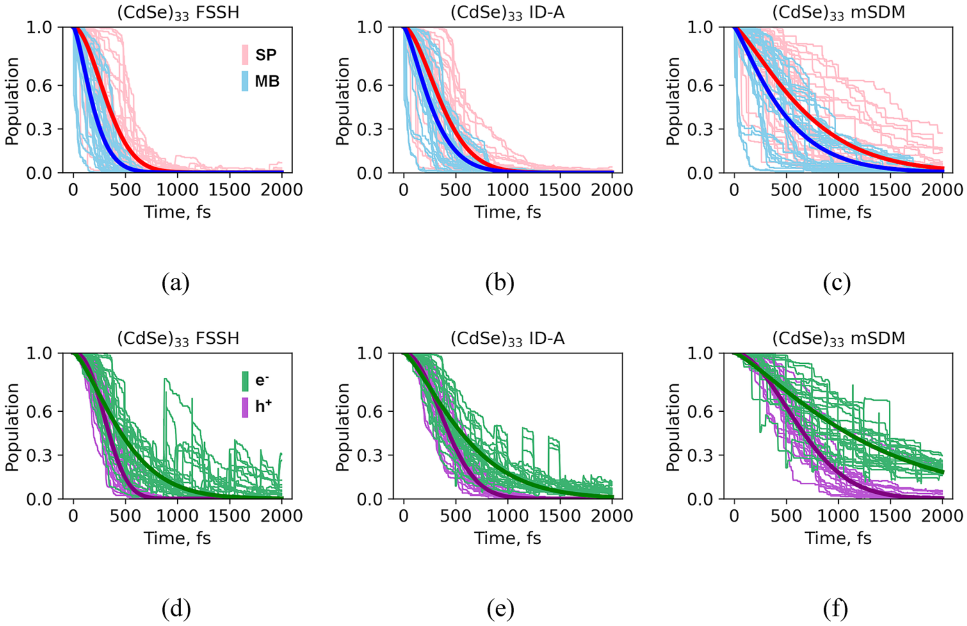

(a) (b) (c)

(d) (e) (f)

Figure 6. Decay of the 1P excitation to 1S excitation in the CdSe NC in the SP and MB dynamical bases: SP with all electron−hole excitations (red lines, a−c), MB (blue lines, a−c), and SP with electron-only (green lines, d−f) or hole-only (purple lines, d−f) excitations. Various TSH approaches are used: FSSH (a, d), ID-A (b, e), and mSDM (c, f). The average population for each case is shown in bold lines, whereas thin lines illustrate the population dynamics for each initial condition (excited state and nuclear trajectory).

population recovery time constants are obtained by fitting the total population of all "hot" excited states to the function eq 20. Such calculations are done separately for each trajectory, which is defined by the initial conditions (starting geometry and the starting individual state—see section 2.6) in order to obtain the error bars for the estimated timescales. The excited state population evolution along each of such trajectories is shown as light thinner lines in Figures 5 and 6. Additionally, the plots of excess excitation energy dissipation are shown in Figures S5 and S6 in the Supporting Information. The latter follow qualitatively the trends in the population decay, so our discussion focuses on the population decay dynamics. The individual curves may vary quite significantly, depending on the details of the starting conditions. The variation of the curve shapes defines the error bars for the computed timescales. We emphasize that the error bars estimated this way are more relevant to the experimental uncertainty. Fitting the averaged populations could lead to mean timescales but would not produce the error bars (other than the error bars for the fitting itself). We found that single or biexponential fitting functions

Table 1. Excited States Population Decay Time Constants, τ (fs), and the Exponential Stretch/Compression Parameters, β (Unitless), Used in the Fitting Function Eq. 20[a]

		FSSH		ID-A		mSDM	
$Si_{75}H_{64}$ (~1.4 nm)		τ	β	τ	β	τ	β
experiment (0.4–1.0 eV)		(495–880 fs, 3.4–7.3 nm),[111] (600 fs, 2–4 nm),[112] and (380–610 fs, 4 nm)[135]					
MB	~0.7 eV	125 ± 19	2.11 ± 0.27	164 ± 24	1.75 ± 0.13	261 ± 43	2.02 ± 0.37
SP, mixed electron−hole	~0.7 eV	344 ± 33	2.52 ± 0.24	399 ± 38	2.28 ± 0.19	836 ± 90	2.02 ± 0.18
SP, electron only	~0.7 eV	252 ± 19	2.03 ± 0.17	293 ± 20	1.76 ± 0.11	700 ± 58	1.56 ± 0.13
SP, hole only	~0.7 eV	196 ± 13	2.43 ± 0.25	231 ± 14	2.10 ± 0.12	557 ± 41	1.52 ± 0.09
		FSSH		ID-A		mSDM	
$Cd_{33}Se_{33}$ (~1.3 nm)		τ	β	τ	β	τ	β
experiment (0.3–0.8 eV)		(300 fs, 2–5.6 nm),[113] (200–530 fs, 2.3–4.1 nm),[136] (<1 ps 0.8–1.4 nm),[137] and (220 fs, 4.2 nm)[138]					
MB	1P → 1S	220 ± 34	2.70 ± 0.67	307 ± 44	2.23 ± 0.46	513 ± 85	2.12 ± 0.40
SP, mixed electron−hole	1P → 1S	376 ± 45	3.41 ± 0.65	421 ± 53	3.15 ± 0.64	761 ± 144	2.56 ± 0.64
SP, electron only	1P → 1S	534 ± 54	2.32 ± 0.85	644 ± 52	1.68 ± 0.28	1291 ± 107	1.37 ± 0.15
SP, hole only	1P → 1S	374 ± 27	2.88 ± 0.37	480 ± 33	2.27 ± 0.18	770 ± 83	2.18 ± 0.23

[a] Approximate diameters of the NCs are given in parentheses.

as well as Gaussian fitting alone do not work for all cases, so we utilized the stretched/compressed exponential function to fit the population decay curves. The quantitative parameters describing the dynamics in two systems are summarized in Table 1.

For both systems, accounting for MB effects leads to a notable acceleration of the dynamics (Figures 5 and 6). On average, the population decay becomes 2−4 times faster in comparison to the dynamics computed using the SP-based mixed electron−hole excitation basis. The degree of acceleration depends on the system (Si vs CdSe) and the methodology used (FSSH vs ID-A or mSDM). The overall acceleration of the excited states' decay in the MB basis is attributed to larger NACs between such states (Figure 4) as well as to the structure of the coupling matrix, which favors more transitions in the MB picture (Figure 3). As such, the depopulation rates depend on the used basis of excited states. To analyze this effect alone (without worrying of how it interplays with decoherence corrections), it is convenient to consider the FSSH results only. Generally, the density of the hole states is larger than the density of the electron states, which is also the case for our systems (Figure 1c,d and also Figures S7 and S8 of the Supporting Information). Thus, the "hole-only" excitation basis generally leads to the smallest timescales for the SP bases (faster dynamics, e.g., 196 fs for Si and 374 fs for CdSe), at least in the comparison to the "electron-only" excitation basis (252 fs for Si and 534 fs for CdSe). This relationship also holds when the decoherence corrections are introduced with either ID-A or mSDM.

The density of the mixed "electron−hole" excitations may vary as a function of state energy, and we observe no clear ordering of the timescales computed in this basis with the timescales computed in the "electron-only" or "hole-only" excitation bases. Depending on the system, the timescales computed in the mixed basis may gravitate toward the timescales computed in one of the bases. Indeed, the timescale for the Si NC (344 fs) is closer to those obtained in the "electron-only" excitation basis, suggesting that the unoccupied (electron) states may introduce larger-than-usual gaps in the basis of mixed "electron−hole" excitations and form bottlenecks in the dynamics (Figures S7 and S8 of the Supporting Information). On the contrary, the timescale for the CdSe NC (376 fs) is closer to those obtained with the "hole-only" excitation basis (374 fs), suggesting that the excited state relaxation dynamics in CdSe may be dominated by the dynamics of holes. These trends still hold qualitatively when decoherence schemes are used, although the differences in the absolute values of the timescales become more notable.

In most cases, the depopulation dynamics follows a compressed Gaussian kinetics ($\beta > 2$). The values of the β parameter may be rationalized by the densities of states in the corresponding bases. A higher density of states favors fast transitions between states, including those upward in energy. In the TSH schemes without decoherence, this leads to the delayed depopulation of the entire band, which in certain cases may manifest itself via an initial plateau in the initial band's population (e.g., Figure 6a). As a result, the larger the density of states, the stronger the depopulation kinetics is compressed (the larger the β >2 value). We also observe a general trend that the dynamics becomes less compressed or even becomes stretched (β<2) when decoherence corrections are included. This effect can be interpreted as follows: decoherence forces the wavefunction to collapse onto the pure quantum states and suppresses the coherent dynamics. As a result, the multitude of the possible "re-excitation" (coherent transfer) channels present in the FSSH dynamics is reduced, leaving only a few pathways for excited state relaxation remaining, which leads to smaller β values.

Accounting for decoherence with either the ID-A or mSDM methods leads to slower excited states decay dynamics, as generally expected.[93] It is worth discussing the observed differences in the ID-A and mSDM timescales. The former is only slightly larger than those computed with the FSSH method. In addition, the β values are consistently smaller in mSDM than in ID-A. Both observations suggest that the mSDM method "forces" the wavefunction to collapse more effectively than the ID-A. We attribute such a difference to the difference in the events that cause the wavefunction collapse. In the ID-A, this is the surface hop itself, which occurs with the rates determined by the original FSSH method. Thus, the coherences may be preserved for a longer time than needed. In the mSDM method, the wavefunction collapses are determined by the pure dephasing time for the pair of states involved in the transition. The timescales are relatively short (typically on the order of 10 fs); thus, the coherences are eliminated with the mSDM more efficiently than by ID-A, leading to smaller β values.

For Si NCs, the timescales computed using MB (Figure 5a–c) and SP (Figure 5d–f) excited states are both consistent with the results of previous computational studies that reported the timescales in the range from 180 to 400 fs.[5,42] Experimental measurements suggest that hot carriers in Si NCs relax on timescales of 380–880 fs.[111,112,135] Regarding the mSDM decoherence scheme as the most advanced / accurate, we find that the NAD with SP-based excited states (in any basis) yields the timescales in the range of 557–836 fs, in an apparent agreement with the experiments.[111,112,135] The decay dynamics with MB-based excitations are still faster than experimental results despite the decoherence corrections being accounted for. Furthermore, considering the role of the size of NCs, one can further find reasons for the difference between experiment and theory. Namely, the Si NC used in our simulations has a diameter of roughly 1.4 nm, whereas the experimentally reported clusters range from 2 to 7.3 nm in diameter. The experiment of Bergren et al.[111] suggests that the relaxation timescales decrease as the size of Si NCs increases. Thus, the experimental timescales shown in Table 1 shall be regarded as the lower bound to the true values one can expect in computations with smaller Si NCs such as ours.

We attribute the above discrepancy in the timescales to the quality of the electronic structure calculations. Since the present work relies on the energies derived from a pure density functional (PBE), the energy gaps may be somewhat underestimated, leading to a slight overestimation of NACs. We anticipate that using the MB basis computed with hybrid density functionals (especially the range-separated ones) could introduce additional electronic exchange terms for more distant KS orbitals. We expect that such terms would decrease the magnitude of NACs (as was already demonstrated in the past at the SP level)[118] and hence would decrease the relaxation rates, shifting the reported timescales toward larger values. Under such circumstances, the timescales obtained at the MB level would come into better agreement with the experiment, whereas the SP-based timescales would become overestimated. Other parameters such as surface capping ligands, surface defects, solvent effects, differences in system sizes, and/or using different dynamical procedures may affect the computed NAD and may need to be accounted for before one relates these timescales to what the experiment yields. Unfortunately, calculations involving larger NC models and the use of hybrid exchange-correlation functionals (especially within TD-DFT) are still computationally demanding and remain an important subject of future studies.

For the CdSe NC, both the MB (Figure 6a–c) and the SP (Figure 6d–f) treatments of the excited states yield subpicosecond timescales. These numbers are consistent with the time-resolved measurements of Klimov,[113,136,137] Singhal,[112] and others[138] suggesting 200–530 fs timescales. The timescales obtained with the FSSH and ID-A methods all fall nicely within the range of the experimentally-determined time constants, with only slight deviations for the "electron-only" excitation basis. The use of MB states instead of SP states does not significantly affect the qualitative trends and the numerical values of the computed parameters. However, when the mSDM methodology is used, the difference between the results obtained using MB vs SP states is more notable. In this case, the use of MB excited states leads to timescales that are in good agreement (513 ± 85 fs) with respect to the upper bound of the experimentally reported values (530 fs). The SP description of excited states (all bases) leads to timescales that are overestimated with respect to the experimental references by nearly 2 times or more. As alluded to earlier, we believe the mSDM scheme may be more reliable way of handling decoherence, since the use of this scheme reduces the β parameter to a greater extent than ID-A. At the same time, the FSSH results should be taken with a grain of salt, since the methodology does not account for electronic decoherence by its construction. Thus, we tend to regard the mSDM results as the most suitable for a direct comparison with experiments.

Having discussed the timescales obtained, it is worth pointing out that the current agreement with the experiment is still partially achieved via a cancellation of errors. As we alluded to in the discussion of the Si NC timescales, the use of hybrid density functionals may increase the gaps between excited states, decrease the corresponding NACs, and slow down the dynamics. However, such effects would likely be balanced if spin–orbit coupling (SOC) is included. As suggested in an earlier study, the inclusion of SOC may greatly accelerate the nonradiative decay dynamics of excited states.[139] Thus, the net effect of not including SOC and a hybrid functional in the calculations may be similar to including both of them. Thus, the use of MB wavefunctions could still be beneficial in comparison to using their SP-based counterparts, bringing the computed timescales in closer agreement with the experiment.

As mentioned in the discussion of the Si NC timescales, accounting for the effects of the NC size and morphology may be important in making a balanced comparison. The size of the CdSe NC considered herein is roughly 1.3 nm in diameter, within the 0.8–5.6 nm diameter range accessible in the experiments. Thus, the theory–experiment comparison is quite reasonable in this regard. Finally, we also note that although the timescales computed with the SP excited states are overestimated in comparison to the experimentally reported times, they are consistent with the roughly 1 ps timescales reported by previous computational studies conducted also at the SP level.[91,140–142]

As our calculations for both Si and CdSe NCs suggest, the dynamics in the special "electron-only" or "hole-only" excitation bases may be more similar to the dynamics in the MB basis than it is in the SP-based mixed "electron–hole" excitation basis. At this point, we believe this agreement may likely be a numerical coincidence rather than a systematic trend, and it is sensitive to the type of system used as well as to the dynamical methodology (FSSH or other TSH schemes). Considering that the mixed "electron–hole" excitation basis is more complete than any of the more specialized "electron-only" or "hole-only" excitation bases, one could expect the mixed excitation basis to yield a better agreement with the MB-based dynamics. The better performance of the specialized bases is then attributed to the difference in the structure of the NAC matrices between the two types of bases. In the electron-only and hole-only bases, nearby states are coupled to each other, leading to a diagonal-looking structure of the NAC matrix. This situation holds qualitatively in the MB basis as well, although the more distant excitations can be coupled too due to a mixing of the Slater-determinant excitations in the TD-DFT wavefunctions. However, the structure of the NAC matrix remains diagonally dominated. In the mixed electron–hole excitation basis, the energy ordering of excited states makes the coupling matrix appear scattered. The energetically close states (coupled both in the MB basis and in the SP-based specialized bases) may become decoupled, whereas energetically distant states may be coupled. As a consequence, the dynamics in the mixed electron−hole excitation basis may become notably different from that in other bases. Having said that, we do not expect the specialized "electron-only" and "hole-only" excitation bases to yield a good agreement with the MB-based dynamics systematically. However, we believe a variety of the previously reported studies that relied on a SP description of the excited states in which the specialized "electron-only" or "hole-only" were utilized and reported to be in good agreement with the experimental data, might have been fortunate to take advantage of the NAC matrix structure effect described above.

3.4. Performance Analysis. To provide an estimate of the computational efficiency of the developed protocol, we summarize the computational times for key components of the calculations, namely, for performing KS-DFT and linear-response TD-DFT calculations, processing the generated cube files, and computing the time overlaps (Table 2). Our benchmarks show that the linear-response TD-DFT calculations constitute the most time-consuming part of the workflow. The KS-DFT calculations are an order of magnitude faster than the linear-response TD-DFT calculations for both systems. Both types of calculations are standard components of the CP2K package, so these tests are primarily meant to provide an estimate of the time required to study comparable systems by an interested user and do not reflect the efficiency of our new workflow. Our scalability tests demonstrate a reasonable scaling of the electronic structure calculation part up to 16 processors for the CdSe NC and up to 32 CPUs for the Si NC.

The reading of the "cube" files and the time-overlap calculations based on processing these "cube" files can constitute 20−50% of the KS-DFT time, which may be a sizable overhead if one chooses to stay at the SP description of the excited states, but is only a negligible fraction of the TD-DFT costs, if one wishes to go beyond the SP picture. The sizable timings of the "cube" file processing originate from the need to process many such files (50 in these tests). As mentioned above, the "cube" files are read utilizing the multiprocessing features of the corresponding Python libraries. We observe that the reading of the "cube" files is indeed notably accelerated by the use of the multiprocessing Python library and reasonably scales up to 16 CPUs. We attribute the scalability limits to the size of the systems studied considering that even larger systems will naturally increase the computing times. Therefore, the use of parallelization will be more critical, and one may achieve a better scalability. At this point, the computation of the time-overlaps via a numerical integration procedure does not scale well and is limited to a single CPU efficiency. The scalability of this step will be addressed in the future releases and updates of the current code.

Table 2. Performance Assessment of the Developed Computational Workflow[a]

system Info	$Cd_{33}Se_{33}$; TD-DFT states = 30; KS orbitals = 50			$Si_{75}H_{64}$; TD-DFT states = 50; KS orbitals = 50		
number of CPUs	4	16	32	4	16	32
KS-SCF	116.6	49.7	45.1	276.4	124.6	70.7
TD-DFPT	2118.9	885	818	7903	3619.9	1978.8
"cube" reading	13.35	4.42	4.83	26.32	8.6	6.2
"cube" overlap	10.56	10.93	15.29	27.75	27.25	29.99

[a] Times are given in seconds and correspond to single-point calculations (one integration timestep). Computations are done using an Intel(R) Xeon(R) Gold 6130 CPU @ 2.10GHz - 32 core/node machine. Timings for "cube" file processing (reading and overlap computations) are computed as the timings to handle 50 files.

4. SUMMARY AND CONCLUSIONS

In this work, we present a new computational scheme that can account for MB effects when modeling NAD in nanoscale and condensed matter systems. The approach is available as part of the open-source modular Libra software package, v4.9.1.[143] The developed dynamical scheme can be used with any electronic structure code that can produce the "cube" files and export the excited Slater determinant amplitudes in the CI superposition describing excited states. Our current version uses LR-TD-DFT wavefunctions as computed via the CP2K package but can be easily used with other electronic structure methods and codes. Presently, working interfaces with the DFTB+ and Gaussian codes are available and their applications will be documented in the future.

We find that the use of MB wavefunctions qualitatively changes the structure of the NAC matrices in comparison to those obtained at the SP level. At the MB level, the energetically distant states may be strongly coupled to each other due to the strong coupling of the underlying SDs present in the MB wavefunctions. At the SP level, the energetically distant states may be coupled, whereas the adjacent states may remain uncoupled. The structure of the coupling matrix in the SP excitation basis is attributed to the diabatic character of the corresponding SD states and the neglect of interaction between them, which enables frequent trivial crossings of such states. On average, the NACs in the MB basis are shifted toward larger magnitudes than those computed in the corresponding SP-based electron−hole excitation basis.

We demonstrate the utility of our computational approach by modeling the phonon-assisted excited states relaxation dynamics in Si and CdSe NCs at both the MB and SP descriptions of excited electronic states. Generally, the use of the MB states accelerates the NAD in comparison to the dynamics computed in the extensive basis of single-determinantal "mixed electron−hole" excitations. The relaxation of hot carriers in the Si NC repopulates two lowest excited states within 125 (FSSH), 164 (ID-A), and 261 (mSDM) fs at the MB level as opposed to 344 (FSSH), 399 (ID-A), and 836 (mSDM) fs at the SP level. The timescales computed with both MB and SP approaches are in agreement with the sub-picosecond high-energy excited state relaxation time for Si NC reported experimentally.[111,112,135] For the CdSe NC, the use of MB states leads to 220 (FSSH), 307 (ID-A), and 513 (mSDM) fs timescales as opposed to 376 (FSSH), 421 (ID-A), and 761 (mSDM) fs at the SP level, bringing the computed timescales in excellent agreement with the available experimental data of ca. 200−530 fs.[113,136−138] For both systems, the MB treatment of excited states consistently predicts faster relaxation than the SP approach does. Whereas this effect is less straightforward to interpret for Si NCs, the use of MB excited states in CdSe does help obtain a better agreement of computed timescales with those reported experimentally. The detailed input, outputs, and other data files for such calculations are available via Zenodo.[144]

Based on the analysis of the dynamics computed with different types of dynamical bases, we conclude that the SP approximation should be used with care, especially if one considers an exhaustive basis of all "electron−hole" excitations. In such a basis, the transitions pathways determined by the hole and electron dynamics would be put on equal footing. In reality (e.g., coming from the analysis of the SD amplitudes in the MB excited states), the contributions of electron vs hole transitions may vary depending on the identities of the considered excited states. Consequently, if the MB states are composed of excitations into a variety of unoccupied electronic states from a limited number of occupied states, the use of an "electron-only" excitation basis may be justified. Analogous logic holds to justify the use of a "hole-only basis". In fact, our present calculations support the idea that the excited state dynamics in the CdSe NC is dominated by the hole dynamics and such a "hole-only" excitation basis might be the most appropriate. For both scenarios described above, the use of a dynamical basis that includes multiple "electron−hole" excitation states would be unjustified since the resulting dynamics would reflect the evolution of single-particle excitations that may not be present in the true MB states.

■ ASSOCIATED CONTENT

Supporting Information

The Supporting Information is available free of charge at https://pubs.acs.org/doi/10.1021/acs.jctc.0c01009.

Further details on the use and generation of Gaussian cube files, state tracking algorithm, phase correction algorithm, as well as time-averaged nonadiabatic couplings in the "electron-only" and "hole-only" excitation bases, and energy levels vs time for the "electron-only", "hole-only", mixed "electron−hole", and TD-DFT excited states (PDF)

Evolution of the KS orbitals in the Si NC with phase correction (MP4)

Evolution of the KS orbitals in the Si NC without phase correction (MP4)

■ AUTHOR INFORMATION

Corresponding Author

Alexey V. Akimov − *Department of Chemistry, University at Buffalo, The State University of New York, Buffalo, New York 14260, United States;* orcid.org/0000-0002-7815-3731; Email: alexeyak@buffalo.edu

Authors

Brendan Smith − *Department of Chemistry, University at Buffalo, The State University of New York, Buffalo, New York 14260, United States;* orcid.org/0000-0003-3460-9984

Mohammad Shakiba − *Department of Materials Science and Engineering, Shahid Bahonar University of Kerman, Kerman 76169-14111, Iran*

Complete contact information is available at: https://pubs.acs.org/10.1021/acs.jctc.0c01009

Author Contributions

[§]B.S. and M.S. contributed equally. The manuscript was written through contributions of all authors. All authors have given approval to the final version of the manuscript.

Funding

A.V.A. acknowledges the financial support of the National Science Foundation (Grant OAC-NSF-1931366). M.S. acknowledges financial support from Shahid Bahonar University of Kerman.

Notes

The authors declare no competing financial interest.

■ ACKNOWLEDGMENTS

Support for the computations is provided by the Center for Computational Research at the University at Buffalo.

■ REFERENCES

(1) Guo, H.; Chu, W.; Zheng, Q.; Zhao, J. Tuning the Carrier Lifetime in Black Phosphorene through Family Atom Doping. *J. Phys. Chem. Lett.* **2020**, *11*, 4662−4667.

(2) Tian, Y.; Zheng, Q.; Zhao, J. Tensile Strain-Controlled Photogenerated Carrier Dynamics at the van Der Waals Heterostructure Interface. *J. Phys. Chem. Lett.* **2020**, *11*, 586−590.

(3) Chu, W.; Saidi, W. A.; Zhao, J.; Prezhdo, O. V. Soft Lattice and Defect Covalency Rationalize Tolerance of β-$CsPbI_3$ Perovskite Solar Cells to Native Defects. *Angew. Chem., Int. Ed.* **2020**, *59*, 6435−6441.

(4) He, J.; Casanova, D.; Fang, W.-H.; Long, R.; Prezhdo, O. V. MAI Termination Favors Efficient Hole Extraction and Slow Charge Recombination at $MAPbI_3$/CuSCN Heterojunction. *J. Phys. Chem. Lett.* **2020**, *11*, 4481−4489.

(5) Smith, B.; Akimov, A. V. Hot Electron Cooling in Silicon Nanoclusters via Landau−Zener Nonadiabatic Molecular Dynamics: Size Dependence and Role of Surface Termination. *J. Phys. Chem. Lett.* **2020**, *11*, 1456−1465.

(6) Madjet, M. E.; Berdiyorov, G. R.; El-Mellouhi, F.; Alharbi, F. H.; Akimov, A. V.; Kais, S. Cation Effect on Hot Carrier Cooling in Halide Perovskite Materials. *J. Phys. Chem. Lett.* **2017**, *8*, 4439−4445.

(7) Yazdani, N.; Bozyigit, D.; Vuttivorakulchai, K.; Luisier, M.; Infante, I.; Wood, V. Tuning Electron−Phonon Interactions in Nanocrystals through Surface Termination. *Nano Lett.* **2018**, *18*, 2233−2242.

(8) Grimaldi, G.; Crisp, R. W.; ten Brinck, S.; Zapata, F.; van Ouwendorp, M.; Renaud, N.; Kirkwood, N.; Evers, W. H.; Kinge, S.; Infante, I.; Siebbeles, L. D. A.; Houtepen, A. J. Hot-Electron Transfer in Quantum-Dot Heterojunction Films. *Nat. Commun.* **2018**, *9*, 2310.

(9) Boehme, S. C.; ten Brinck, S.; Maes, J.; Yazdani, N.; Zapata, F.; Chen, K.; Wood, V.; Hodgkiss, J. M.; Hens, Z.; Geiregat, P.; Infante, I. Phonon-Mediated and Weakly Size-Dependent Electron and Hole Cooling in $CsPbBr_3$ Nanocrystals Revealed by Atomistic Simulations and Ultrafast Spectroscopy. *Nano Lett.* **2020**, *20*, 1819−1829.

(10) Senanayake, R. D.; Aikens, C. M. Electronic Relaxation Dynamics in $[Au_{25}(SR)_{18}]^{-1}$ (R=CH_3, C_2H_5, C_3H_7, MPA, PET) Thiolate-Protected Nanoclusters. *Phys. Chem. Chem. Phys.* **2020**, *22*, 5272−5285.

(11) Lystrom, L.; Tamukong, P.; Mihaylov, D.; Kilina, S. Phonon-Driven Energy Relaxation in PbS/CdS and PbSe/CdSe Core/Shell Quantum Dots. *J. Phys. Chem. Lett.* **2020**, *11*, 4269−4278.

(12) Forde, A.; Inerbaev, T.; Hobbie, E. K.; Kilin, D. S. Excited-State Dynamics of a $CsPbBr_3$ Nanocrystal Terminated with Binary Ligands: Sparse Density of States with Giant Spin−Orbit Coupling Suppresses Carrier Cooling. *J. Am. Chem. Soc.* **2019**, *141*, 4388−4397.

(13) Senanayake, R. D.; Aikens, C. M. Theoretical Investigation of Relaxation Dynamics in the $Au_{18}(SH)_{14}$ Thiolate-Protected Gold Nanocluster. *J. Chem. Phys.* **2019**, *151*, No. 094702.

(14) Zhang, Z.; He, J.; Long, R. Ultrafast Charge Separation and Recombination across a Molecule/$CsPbBr_3$ Quantum Dot Interface from First-Principles Nonadiabatic Molecular Dynamics Simulation. *J. Phys. Chem. C* **2019**, *123*, 23800−23806.

(15) Habib, M.; Kar, M.; Pal, S.; Sarkar, P. Role of Chalcogens in the Exciton Relaxation Dynamics of Chalcogenol-Functionalized CdSe

QD: A Time-Domain Atomistic Simulation. *Chem. Mater.* **2019**, *31*, 4042−4050.

(16) Long, R.; Liu, J.; Prezhdo, O. V. Unravelling the Effects of Grain Boundary and Chemical Doping on Electron−Hole Recombination in $CH_3NH_3PbI_3$ Perovskite by Time-Domain Atomistic Simulation. *J. Am. Chem. Soc.* **2016**, *138*, 3884−3890.

(17) Long, R.; Prezhdo, O. V. Dopants Control Electron−Hole Recombination at Perovskite−TiO_2 Interfaces: Ab Initio Time-Domain Study. *ACS Nano* **2015**, *9*, 11143−11155.

(18) Liu, J.; Prezhdo, O. V. Chlorine Doping Reduces Electron−Hole Recombination in Lead Iodide Perovskites: Time-Domain Ab Initio Analysis. *J. Phys. Chem. Lett.* **2015**, *6*, 4463−4469.

(19) Long, R.; Fang, W.; Akimov, A. V. Nonradiative Electron−Hole Recombination Rate Is Greatly Reduced by Defects in Monolayer Black Phosphorus: Ab Initio Time Domain Study. *J. Phys. Chem. Lett.* **2016**, *7*, 653−659.

(20) Nie, Z.; Long, R.; Sun, L.; Huang, C.-C.; Zhang, J.; Xiong, Q.; Hewak, D. W.; Shen, Z.; Prezhdo, O. V.; Loh, Z.-H. Ultrafast Carrier Thermalization and Cooling Dynamics in Few-Layer MoS_2. *ACS Nano* **2014**, *8*, 10931−10940.

(21) Nelson, T. R.; White, A. J.; Bjorgaard, J. A.; Sifain, A. E.; Zhang, Y.; Nebgen, B.; Fernandez-Alberti, S.; Mozyrsky, D.; Roitberg, A. E.; Tretiak, S. Non-Adiabatic Excited-State Molecular Dynamics: Theory and Applications for Modeling Photophysics in Extended Molecular Materials. *Chem. Rev.* **2020**, *120*, 2215−2287.

(22) Crespo-Otero, R.; Barbatti, M. Recent Advances and Perspectives on Nonadiabatic Mixed Quantum−Classical Dynamics. *Chem. Rev.* **2018**, *118*, 7026−7068.

(23) Kilina, S.; Kilin, D.; Tretiak, S. Light-Driven and Phonon-Assisted Dynamics in Organic and Semiconductor Nanostructures. *Chem. Rev.* **2015**, *115*, 5929−5978.

(24) Curchod, B. F. E.; Martínez, T. J. Ab Initio Nonadiabatic Quantum Molecular Dynamics. *Chem. Rev.* **2018**, *118*, 3305−3336.

(25) Smith, B.; Akimov, A. V. Modeling Nonadiabatic Dynamics in Condensed Matter Materials: Some Recent Advances and Applications. *J. Phys.: Condens. Matter* **2020**, *32*, No. 073001.

(26) Akimov, A. V.; Neukirch, A. J.; Prezhdo, O. V. Theoretical Insights into Photoinduced Charge Transfer and Catalysis at Oxide Interfaces. *Chem. Rev.* **2013**, *113*, 4496−4565.

(27) Wang, L.; Akimov, A.; Prezhdo, O. V. Recent Progress in Surface Hopping: 2011−2015. *J. Phys. Chem. Lett.* **2016**, *7*, 2100−2112.

(28) Barbatti, M. Nonadiabatic Dynamics with Trajectory Surface Hopping Method. *WIREs Comput. Mol. Sci.* **2011**, *1*, 620−633.

(29) Tully, J. C. Molecular Dynamics with Electronic Transitions. *J. Chem. Phys.* **1990**, *93*, 1061−1071.

(30) Craig, C. F.; Duncan, W. R.; Prezhdo, O. V. Trajectory Surface Hopping in the Time-Dependent Kohn-Sham Approach for Electron-Nuclear Dynamics. *Phys. Rev. Lett.* **2005**, *95*, 163001.

(31) Duncan, W. R.; Craig, C. F.; Prezhdo, O. V. Time-Domain Ab Initio Study of Charge Relaxation and Recombination in Dye-Sensitized TiO_2. *J. Am. Chem. Soc.* **2007**, *129*, 8528−8543.

(32) Prezhdo, O. V.; Duncan, W. R.; Prezhdo, V. V. Photoinduced Electron Dynamics at the Chromophore−Semiconductor Interface: A Time-Domain Ab Initio Perspective. *Prog. Surf. Sci.* **2009**, *84*, 30−68.

(33) Akimov, A. V. Nonadiabatic Molecular Dynamics with Tight-Binding Fragment Molecular Orbitals. *J. Chem. Theory Comput.* **2016**, *12*, 5719−5736.

(34) Akimov, A. V.; Prezhdo, O. V. The PYXAID Program for Non-Adiabatic Molecular Dynamics in Condensed Matter Systems. *J. Chem. Theory Comput.* **2013**, *9*, 4959−4972.

(35) Wong, J. C.; Li, L.; Kanai, Y. Size Dependence and Role of Decoherence in Hot Electron Relaxation within Fluorinated Silicon Quantum Dots: A First-Principles Study. *J. Phys. Chem. C* **2018**, *122*, 29526−29536.

(36) Wang, S.; Guo, R. Relaxation of the Photoexcited Electrons in Chevron-Type Graphene Nanoribbons: Many-Body Theory and Nonadiabatic Molecular Dynamics Modeling. *Carbon* **2017**, *124*, 308−313.

(37) Spencer, J.; Gajdos, F.; Blumberger, J. FOB-SH: Fragment Orbital-Based Surface Hopping for Charge Carrier Transport in Organic and Biological Molecules and Materials. *J. Chem. Phys.* **2016**, *145*, No. 064102.

(38) Carof, A.; Giannini, S.; Blumberger, J. Detailed Balance, Internal Consistency, and Energy Conservation in Fragment Orbital-Based Surface Hopping. *J. Chem. Phys.* **2017**, *147*, 214113.

(39) Liu, J.; Neukirch, A. J.; Prezhdo, O. V. Non-Radiative Electron−Hole Recombination in Silicon Clusters: Ab Initio Non-Adiabatic Molecular Dynamics. *J. Phys. Chem. C* **2014**, *118*, 20702−20709.

(40) Long, R.; English, N. J.; Prezhdo, O. V. Defects Are Needed for Fast Photo-Induced Electron Transfer from a Nanocrystal to a Molecule: Time-Domain *Ab Initio* Analysis. *J. Am. Chem. Soc.* **2013**, *135*, 18892−18900.

(41) Chen, J.; Schmitz, A.; Inerbaev, T.; Meng, Q.; Kilina, S.; Tretiak, S.; Kilin, D. S. First-Principles Study of p-n-Doped Silicon Quantum Dots: Charge Transfer, Energy Dissipation, and Time-Resolved Emission. *J. Phys. Chem. Lett.* **2013**, *4*, 2906−2913.

(42) Reeves, K. G.; Schleife, A.; Correa, A. A.; Kanai, Y. Role of Surface Termination on Hot Electron Relaxation in Silicon Quantum Dots: A First-Principles Dynamics Simulation Study. *Nano Lett.* **2015**, *15*, 6429−6433.

(43) Banerjee, S.; Kang, J.; Zhang, X.; Wang, L.-W. The Effects of Interstitial Iodine in Hybrid Perovskite Hot Carrier Cooling: A Non-Adiabatic Molecular Dynamics Study. *J. Chem. Phys.* **2020**, *152*, No. 091102.

(44) Zheng, F.; Wang, L.-W. Ultrafast Hot Carrier Injection in Au/GaN: The Role of Band Bending and the Interface Band Structure. *J. Phys. Chem. Lett.* **2019**, *10*, 6174−6183.

(45) Pal, S.; Trivedi, D. J.; Akimov, A. V.; Aradi, B.; Frauenheim, T.; Prezhdo, O. V. Nonadiabatic Molecular Dynamics for Thousand Atom Systems: A Tight-Binding Approach toward PYXAID. *J. Chem. Theory Comput.* **2016**, *12*, 1436−1448.

(46) Giannini, S.; Carof, A.; Ellis, M.; Yang, H.; Ziogos, O. G.; Ghosh, S.; Blumberger, J. Quantum Localization and Delocalization of Charge Carriers in Organic Semiconducting Crystals. *Nat. Commun.* **2019**, *10*, 3843.

(47) Blumberger, J. Recent Advances in the Theory and Molecular Simulation of Biological Electron Transfer Reactions. *Chem. Rev.* **2015**, *115*, 11191−11238.

(48) Sato, K.; Pradhan, E.; Asahi, R.; Akimov, A. V. Charge Transfer Dynamics at the Boron Subphthalocyanine Chloride/C_{60} Interface: Non-Adiabatic Dynamics Study with Libra-X. *Phys. Chem. Chem. Phys.* **2018**, *20*, 25275−25294.

(49) Rego, L. G. C.; Bortolini, G. Modulating the Photoisomerization Mechanism of Semiconductor-Bound Azobenzene-Functionalized Compounds. *J. Phys. Chem. C* **2019**, *123*, 5692−5698.

(50) Rego, L. G. C.; Hames, B. C.; Mazon, K. T.; Joswig, J.-O. Intramolecular Polarization Induces Electron−Hole Charge Separation in Light-Harvesting Molecular Triads. *J. Phys. Chem. C* **2014**, *118*, 126−134.

(51) Sifain, A. E.; Bjorgaard, J. A.; Nelson, T. R.; Nebgen, B. T.; White, A. J.; Gifford, B. J.; Gao, D. W.; Prezhdo, O. V.; Fernandez-Alberti, S.; Roitberg, A. E.; Tretiak, S. Photoexcited Nonadiabatic Dynamics of Solvated Push−Pull π-Conjugated Oligomers with the NEXMD Software. *J. Chem. Theory Comput.* **2018**, *14*, 3955−3966.

(52) Sifain, A. E.; Gifford, B. J.; Gao, D. W.; Lystrom, L.; Nelson, T. R.; Tretiak, S. NEXMD Modeling of Photoisomerization Dynamics of 4-Styrylquinoline. *J. Phys. Chem. A* **2018**, *122*, 9403−9411.

(53) Ryabinkin, I. G.; Nagesh, J.; Izmaylov, A. F. Fast Numerical Evaluation of Time-Derivative Non-Adiabatic Couplings for Mixed Quantum-Classical Methods. *J. Phys. Chem. Lett.* **2015**, *6*, 4200−4203.

(54) Zanjanchi, F.; Beheshtian, J. Natural Pigments in Dye-Sensitized Solar Cell (DSSC): A DFT-TDDFT Study. *J. Iran. Chem. Soc.* **2019**, *16*, 795−805.

(55) Yang, Z.; Liu, Y.; Liu, C.; Lin, C.; Shao, C. TDDFT Screening Auxiliary Withdrawing Group and Design the Novel D-A-π-A Organic

Dyes Based on Indoline Dye for Highly Efficient Dye-Sensitized Solar Cells. *Spectrochim. Acta, Part A* **2016**, *167*, 127−133.

(56) Gao, Y.; Zhou, B.; Kang, S.-g.; Xin, M.; Yang, P.; Dai, X.; Wang, Z.; Zhou, R. Effect of Ligands on the Characteristics of $(CdSe)_{13}$ Quantum Dots. *RSC Adv.* **2014**, *4*, 27146−27151.

(57) Goel, S.; Velizhanin, K. A.; Piryatinski, A.; Ivanov, S. A.; Tretiak, S. Ligand Effects on Optical Properties of Small Gold Clusters: A TDDFT Study. *J. Phys. Chem. C* **2012**, *116*, 3242−3249.

(58) Alwarappan, G.; Alam, M. R.; Hassan, W. M. I.; Shibl, M. F.; Alfalah, S.; Patil, S.; Nekovei, R.; Verma, A. Role of Organic Cation in Modern Lead-Based Perovskites. *Sol. Energy* **2019**, *189*, 86−93.

(59) Quarti, C.; Marchal, N.; Beljonne, D. Tuning the Optoelectronic Properties of Two-Dimensional Hybrid Perovskite Semiconductors with Alkyl Chain Spacers. *J. Phys. Chem. Lett.* **2018**, *9*, 3416−3424.

(60) Barbatti, M.; Granucci, G.; Persico, M.; Ruckenbauer, M.; Vazdar, M.; Eckert-Maksić, M.; Lischka, H. The On-the-Fly Surface-Hopping Program System Newton-X: Application to Ab Initio Simulation of the Nonadiabatic Photodynamics of Benchmark Systems. *J. Photochem. Photobiol., A* **2007**, *190*, 228−240.

(61) Richter, M.; Marquetand, P.; González-Vázquez, J.; Sola, I.; González, L. SHARC: Ab Initio Molecular Dynamics with Surface Hopping in the Adiabatic Representation Including Arbitrary Couplings. *J. Chem. Theory Comput.* **2011**, *7*, 1253−1258.

(62) Huang, T.; Lewis, D. K.; Sharifzadeh, S. Assessing the Role of Intermolecular Interactions in a Perylene-Based Nanowire Using First-Principles Many-Body Perturbation Theory. *J. Phys. Chem. Lett.* **2019**, *10*, 2842−2848.

(63) Wetherell, J.; Hodgson, M. J. P.; Talirz, L.; Godby, R. W. Advantageous Nearsightedness of Many-Body Perturbation Theory Contrasted with Kohn-Sham Density Functional Theory. *Phys. Rev. B* **2019**, *99*, No. 045129.

(64) Lewis, D. K.; Sharifzadeh, S. Defect-Induced Exciton Localization in Bulk Gallium Nitride from Many-Body Perturbation Theory. *Phys. Rev. Mater.* **2019**, *3*, 114601.

(65) Sharifzadeh, S. Many-Body Perturbation Theory for Understanding Optical Excitations in Organic Molecules and Solids. *J. Phys.: Condens. Matter* **2018**, *30*, 153002.

(66) Xuan, F.; Chen, Y.; Quek, S. Y. Quasiparticle Levels at Large Interface Systems from Many-Body Perturbation Theory: The XAF-GW Method. *J. Chem. Theory Comput.* **2019**, *15*, 3824−3835.

(67) Lewis, D. K.; Matsubara, M.; Bellotti, E.; Sharifzadeh, S. Quasiparticle and Hybrid Density Functional Methods in Defect Studies: An Application to the Nitrogen Vacancy in GaN. *Phys. Rev. B* **2017**, *96*, 235203.

(68) Tapavicza, E.; Tavernelli, I.; Rothlisberger, U. Trajectory Surface Hopping within Linear Response Time-Dependent Density-Functional Theory. *Phys. Rev. Lett.* **2007**, *98*, No. 023001.

(69) Niehaus, T. A.; Suhai, S.; Della Sala, F.; Lugli, P.; Elstner, M.; Seifert, G.; Frauenheim, T. Tight-Binding Approach to Time-Dependent Density-Functional Response Theory. *Phys. Rev. B* **2001**, *63*, No. 085108.

(70) Hourahine, B.; Aradi, B.; Blum, V.; Bonafé, F.; Buccheri, A.; Camacho, C.; Cevallos, C.; Deshaye, M. Y.; Dumitrică, T.; Dominguez, A.; Ehlert, S.; Elstner, M.; van der Heide, T.; Hermann, J.; Irle, S.; Kranz, J. J.; Köhler, C.; Kowalczyk, T.; Kubař, T.; Lee, I. S.; Lutsker, V.; Maurer, R. J.; Min, S. K.; Mitchell, I.; Negre, C.; Niehaus, T. A.; Niklasson, A. M. N.; Page, A. J.; Pecchia, A.; Penazzi, G.; Persson, M. P.; Řezáč, J.; Sánchez, C. G.; Sternberg, M.; Stöhr, M.; Stuckenberg, F.; Tkatchenko, A.; Yu, V. W. -z.; Frauenheim, T. DFTB+, a Software Package for Efficient Approximate Density Functional Theory Based Atomistic Simulations. *J. Chem. Phys.* **2020**, *152*, 124101.

(71) Aradi, B.; Hourahine, B.; Frauenheim, T. DFTB+, a Sparse Matrix-Based Implementation of the DFTB Method. *J. Phys. Chem. A* **2007**, *111*, 5678−5684.

(72) Humeniuk, A.; Mitrić, R. DFTBaby: A Software Package for Non-Adiabatic Molecular Dynamics Simulations Based on Long-Range Corrected Tight-Binding TD-DFT(B). *Comput. Phys. Commun.* **2017**, *221*, 174−202.

(73) Lewis, J. P.; Jelínek, P.; Ortega, J.; Demkov, A. A.; Trabada, D. G.; Haycock, B.; Wang, H.; Adams, G.; Tomfohr, J. K.; Abad, E.; Wang, H.; Drabold, D. A. Advances and Applications in the FIREBALLab Initio Tight-Binding Molecular-Dynamics Formalism. *Phys. Status Solidi B* **2011**, *248*, 1989−2007.

(74) Tretiak, S.; Chernyak, V.; Mukamel, S. Collective Electronic Oscillators for Nonlinear Optical Response of Conjugated Molecules. *Chem. Phys. Lett.* **1996**, *259*, 55−61.

(75) Tretiak, S.; Chernyak, V.; Mukamel, S. Two-Dimensional Real-Space Analysis of Optical Excitations in Acceptor-Substituted Carotenoids. *J. Am. Chem. Soc.* **1997**, *119*, 11408−11419.

(76) Tretiak, S.; Mukamel, S. Density Matrix Analysis and Simulation of Electronic Excitations in Conjugated and Aggregated Molecules. *Chem. Rev.* **2002**, *102*, 3171−3212.

(77) Senanayake, R. D.; Guidez, E. B.; Neukirch, A. J.; Prezhdo, O. V.; Aikens, C. M. Theoretical Investigation of Relaxation Dynamics in $Au_{38}(SH)_{24}$ Thiolate-Protected Gold Nanoclusters. *J. Phys. Chem. C* **2018**, *122*, 16380−16388.

(78) Akimov, A. V.; Prezhdo, O. V. Advanced Capabilities of the PYXAID Program: Integration Schemes, Decoherence Effects, Multiexcitonic States, and Field-Matter Interaction. *J. Chem. Theory Comput.* **2014**, *10*, 789−804.

(79) Zheng, Q.; Chu, W.; Zhao, C.; Zhang, L.; Guo, H.; Wang, Y.; Jiang, X.; Zhao, J. Ab Initio Nonadiabatic Molecular Dynamics Investigations on the Excited Carriers in Condensed Matter Systems. *WIREs Comput. Mol. Sci.* **2019**, *9*, No. e1411.

(80) Ma, J.; Wang, L.-W. The Nature of Electron Mobility in Hybrid Perovskite $CH_3NH_3PbI_3$. *Nano Lett.* **2017**, *17*, 3646−3654.

(81) Li, L.; Kanai, Y. Dependence of Hot Electron Transfer on Surface Coverage and Adsorbate Species at Semiconductor−Molecule Interfaces. *Phys. Chem. Chem. Phys.* **2018**, *20*, 12986−12991.

(82) Senanayake, R. D.; Akimov, A. V.; Aikens, C. M. Theoretical Investigation of Electron and Nuclear Dynamics in the $[Au_{25}(SH)_{18}]^{-1}$ Thiolate-Protected Gold Nanocluster. *J. Phys. Chem. C* **2017**, *121*, 10653−10662.

(83) Elward, J. M.; Chakraborty, A. Effect of Heterojunction on Exciton Binding Energy and Electron−Hole Recombination Probability in CdSe/ZnS Quantum Dots. *J. Chem. Theory Comput.* **2015**, *11*, 462−471.

(84) Elward, J. M.; Chakraborty, A. Effect of Dot Size on Exciton Binding Energy and Electron−Hole Recombination Probability in CdSe Quantum Dots. *J. Chem. Theory Comput.* **2013**, *9*, 4351−4359.

(85) Blanton, C. J.; Brenon, C.; Chakraborty, A. Development of Polaron-Transformed Explicitly Correlated Full Configuration Interaction Method for Investigation of Quantum-Confined Stark Effect in GaAs Quantum Dots. *J. Chem. Phys.* **2013**, *138*, No. 054114.

(86) Elward, J. M.; Thallinger, B.; Chakraborty, A. Calculation of Electron-Hole Recombination Probability Using Explicitly Correlated Hartree-Fock Method. *J. Chem. Phys.* **2012**, *136*, 124105.

(87) Akimov, A. V. Libra: An Open-Source "Methodology Discovery" Library for Quantum and Classical Dynamics Simulations. *J. Comput. Chem.* **2016**, *37*, 1626−1649.

(88) Hutter, J.; Iannuzzi, M.; Schiffmann, F.; VandeVondele, J. CP2K: Atomistic Simulations of Condensed Matter Systems. *WIREs Comput. Mol. Sci.* **2014**, *4*, 15−25.

(89) Kühne, T. D.; Iannuzzi, M.; Del Ben, M.; Rybkin, V. V.; Seewald, P.; Stein, F.; Laino, T.; Khaliullin, R. Z.; Schütt, O.; Schiffmann, F.; Golze, D.; Wilhelm, J.; Chulkov, S.; Bani-Hashemian, M. H.; Weber, V.; Borštnik, U.; Taillefumier, M.; Jakobovits, A. S.; Lazzaro, A.; Pabst, H.; Müller, T.; Schade, R.; Guidon, M.; Andermatt, S.; Holmberg, N.; Schenter, G. K.; Hehn, A.; Bussy, A.; Belleflamme, F.; Tabacchi, G.; Glöß, A.; Lass, M.; Bethune, I.; Mundy, C. J.; Plessl, C.; Watkins, M.; VandeVondele, J.; Krack, M.; Hutter, J. CP2K: An Electronic Structure and Molecular Dynamics Software Package - Quickstep: Efficient and Accurate Electronic Structure Calculations. *J. Chem. Phys.* **2020**, *152*, 194103.

(90) Nikitin, E. E. *Theory of Elementary Atomic and Molecular Processes in Gases*; Clarendon Press: Oxford, 1974.

(91) Akimov, A. V.; Trivedi, D.; Wang, L.; Prezhdo, O. V. Analysis of the Trajectory Surface Hopping Method from the Markov State Model Perspective. *J. Phys. Soc. Jpn.* **2015**, *84*, No. 094002.

(92) Wang, L.; Trivedi, D.; Prezhdo, O. V. Global Flux Surface Hopping Approach for Mixed Quantum-Classical Dynamics. *J. Chem. Theory Comput.* **2014**, *10*, 3598−3605.

(93) Smith, B.; Akimov, A. V. A Comparative Analysis of Surface Hopping Acceptance and Decoherence Algorithms within the Neglect of Back-Reaction Approximation. *J. Chem. Phys.* **2019**, *151*, 124107.

(94) Jaeger, H. M.; Fischer, S.; Prezhdo, O. V. Decoherence-Induced Surface Hopping. *J. Chem. Phys.* **2012**, *137*, 22A545.

(95) Granucci, G.; Persico, M.; Zoccante, A. Including Quantum Decoherence in Surface Hopping. *J. Chem. Phys.* **2010**, *133*, 134111.

(96) Nelson, T.; Fernandez-Alberti, S.; Roitberg, A. E.; Tretiak, S. Nonadiabatic Excited-State Molecular Dynamics: Treatment of Electronic Decoherence. *J. Chem. Phys.* **2013**, *138*, 224111.

(97) Hammes-Schiffer, S.; Tully, J. C. Proton Transfer in Solution: Molecular Dynamics with Quantum Transitions. *J. Chem. Phys.* **1994**, *101*, 4657−4667.

(98) Löwdin, P.-O. Quantum Theory of Many-Particle Systems. I. Physical Interpretations by Means of Density Matrices, Natural Spin-Orbitals, and Convergence Problems in the Method of Configurational Interaction. *Phys. Rev.* **1955**, *97*, 1474.

(99) Farazdel, A.; Dupuis, M.; Clementi, E.; Aviram, A. Electric-Field Induced Intramolecular Electron Transfer in Spiro .Pi.-Electron Systems and Their Suitability as Molecular Electronic Devices. A Theoretical Study. *J. Am. Chem. Soc.* **1990**, *112*, 4206−4214.

(100) Frisch, M. J.; Trucks, G. W.; Schlegel, H. B.; Scuseria, G. E.; Robb, M. A.; Cheeseman, J. R.; Scalmani, G.; Barone, V.; Mennucci, B.; Petersson, G. A.; Nakatsuji, H.; Caricato, M.; Li, X.; Hratchian, H.P.; Izmaylov, A. F.; Bloino, J.; Zheng, G.; Sonnenberg, J. L.; Hada, M.; Ehara, M.; Toyota, K.; Fukuda, R.; Hasegawa, J.; Ishida, M.; Nakajima, T.; Honda, Y.; Kitao, O.; Nakai, H.; Vreven, T.; Montgomery, J. A., Jr.; Peralta, J. E.; Ogliaro, F.; Bearpark, M.; Heyd, J. J.; Brothers, E.; Kudin, K. N.; Staroverov, V. N.; Kobayashi, R.; Normand, J.; Raghavachari, K.; Rendell, A.; Burant, J. C.; Iyengar, S. S.; Tomasi, J.; Cossi, M.; Rega, N.; Millam, J. M.; Klene, M.; Knox, J. E.; Cross, J. B.; Bakken, V.; Adamo, C.; Jaramillo, J.; Gomperts, R.; Stratmann, R. E.; Yazyev, O.; Austin, A. J.; Cammi, R.; Pomelli, C.; Ochterski, J. W.; Martin, R. L.; Morokuma, K.; Zakrzewski, V. G.; Voth, G. A.; Salvador, P.; Dannenberg, J. J.; Dapprich, S.; Daniels, A. D.; Farkas, O.; Foresman, J. B.; Ortiz, J. V.; Cioslowski, J.; Fox, D. J. *Gaussian 09*; Revision D.01.Gaussian, Inc.: 2009.

(101) Zapata, F.; Ridder, L.; Hidding, J.; Jacob, C. R.; Infante, I.; Visscher, L. QMflows: A Tool Kit for Interoperable Parallel Workflows in Quantum Chemistry. *J. Chem. Inf. Model.* **2019**, *59*, 3191−3197.

(102) Pradhan, E.; Sato, K.; Akimov, A. V. Non-Adiabatic Molecular Dynamics with ΔSCF Excited States. *J. Phys.: Condens. Matter* **2018**, *30*, 484002.

(103) Fernandez-Alberti, S.; Roitberg, A. E.; Nelson, T.; Tretiak, S. Identification of Unavoided Crossings in Nonadiabatic Photoexcited Dynamics Involving Multiple Electronic States in Polyatomic Conjugated Molecules. *J. Chem. Phys.* **2012**, *137*, No. 014512.

(104) Wang, L.; Prezhdo, O. V. A Simple Solution to the Trivial Crossing Problem in Surface Hopping. *J. Phys. Chem. Lett.* **2014**, *5*, 713−719.

(105) Qiu, J.; Bai, X.; Wang, L. Crossing Classified and Corrected Fewest Switches Surface Hopping. *J. Phys. Chem. Lett.* **2018**, *9*, 4319−4325.

(106) Akimov, A. V. A Simple Phase Correction Makes a Big Difference in Nonadiabatic Molecular Dynamics. *J. Phys. Chem. Lett.* **2018**, *9*, 6096−6102.

(107) Avramov, P. V.; Fedorov, D. G.; Sorokin, P. B.; Chernozatonskii, L. A.; Gordon, M. S. Atomic and Electronic Structure of New Hollow-Based Symmetric Families of Silicon Nanoclusters. *J. Phys. Chem. C* **2007**, *111*, 18824−18830.

(108) Kasuya, A.; Sivamohan, R.; Barnakov, Y. A.; Dmitruk, I. M.; Nirasawa, T.; Romanyuk, V. R.; Kumar, V.; Mamykin, S. V.; Tohji, K.; Jeyadevan, B.; Shinoda, K.; Kudo, T.; Terasaki, O.; Liu, Z.; Belosludov, R. V.; Sundararajan, V.; Kawazoe, Y. Ultra-Stable Nanoparticles of CdSe Revealed from Mass Spectrometry. *Nat. Mater.* **2004**, *3*, 99−102.

(109) Kilina, S.; Habenicht, B. F. *Excitonic and Vibrational Dynamics in Nanotechnology*; Pan Stanford Publishing: 2009.

(110) Singhal, P.; Ghosh, H. N. Hot Charge Carrier Extraction from Semiconductor Quantum Dots. *J. Phys. Chem. C* **2018**, *122*, 17586−17600.

(111) Bergren, M. R.; Palomaki, P. K. B.; Neale, N. R.; Furtak, T. E.; Beard, M. C. Size-Dependent Exciton Formation Dynamics in Colloidal Silicon Quantum Dots. *ACS Nano* **2016**, *10*, 2316−2323.

(112) Cimpean, C.; Groenewegen, V.; Kuntermann, V.; Sommer, A.; Kryschi, C. Ultrafast Exciton Relaxation Dynamics in Silicon Quantum Dots. *Laser Photonics Rev.* **2009**, *3*, 138−145.

(113) Klimov, V. I.; McBranch, D. W. Femtosecond 1P-to-1S Electron Relaxation in Strongly Confined Semiconductor Nanocrystals. *Phys. Rev. Lett.* **1998**, *80*, 4028−4031.

(114) Park, N.-M.; Kim, T.-S.; Park, S.-J. Band Gap Engineering of Amorphous Silicon Quantum Dots for Light-Emitting Diodes. *Appl. Phys. Lett.* **2001**, *78*, 2575−2577.

(115) Mavros, M. G.; Micha, D. A.; Kilin, D. S. Optical Properties of Doped Silicon Quantum Dots with Crystalline and Amorphous Structures. *J. Phys. Chem. C* **2011**, *115*, 19529−19537.

(116) Bokareva, O. S.; Shibl, M. F.; Al-Marri, M. J.; Pullerits, T.; Kühn, O. Optimized Long-Range Corrected Density Functionals for Electronic and Optical Properties of Bare and Ligated CdSe Quantum Dots. *J. Chem. Theory Comput.* **2017**, *13*, 110−116.

(117) Kilina, S.; Ivanov, S.; Tretiak, S. Effect of Surface Ligands on Optical and Electronic Spectra of Semiconductor Nanoclusters. *J. Am. Chem. Soc.* **2009**, *131*, 7717−7726.

(118) Lin, Y.; Akimov, A. V. Dependence of Nonadiabatic Couplings with Kohn−Sham Orbitals on the Choice of Density Functional: Pure vs Hybrid. *J. Phys. Chem. A* **2016**, *120*, 9028−9041.

(119) Isborn, C. M.; Kilina, S. V.; Li, X.; Prezhdo, O. V. Generation of Multiple Excitons in PbSe and CdSe Quantum Dots by Direct Photoexcitation: First-Principles Calculations on Small PbSe and CdSe Clusters. *J. Phys. Chem. C* **2008**, *112*, 18291−18294.

(120) Izmaylov, A. F.; Scuseria, G. E. Why Are Time-Dependent Density Functional Theory Excitations in Solids Equal to Band Structure Energy Gaps for Semilocal Functionals, and How Does Nonlocal Hartree−Fock-Type Exchange Introduce Excitonic Effects? *J. Chem. Phys.* **2008**, *129*, No. 034101.

(121) Akimov, A. V.; Asahi, R.; Jinnouchi, R.; Prezhdo, O. V. What Makes the Photocatalytic CO_2 Reduction on N-Doped Ta_2O_5 Efficient: Insights from Nonadiabatic Molecular Dynamics. *J. Am. Chem. Soc.* **2015**, *137*, 11517−11525.

(122) Madjet, M. E.-A.; Akimov, A. V.; El-Mellouhi, F.; Berdiyorov, G. R.; Ashhab, S.; Tabet, N.; Kais, S. Enhancing the Carrier Thermalization Time in Organometallic Perovskites by Halide Mixing. *Phys. Chem. Chem. Phys.* **2016**, *18*, 5219−5231.

(123) Yan, H.; Li, Y.; Li, X.; Wang, B.; Li, M. Hot Carrier Relaxation in $Cs_2TiI_yBr_{6-y}$ (y=0, 2 and 6) by a Time-Domain Ab Initio Study. *RSC Adv.* **2020**, *10*, 958−964.

(124) Zhang, S.-F.; Chen, X.-K.; Ren, A.-M.; Li, H.; Bredas, J.-L. Impact of Organic Spacers on the Carrier Dynamics in 2D Hybrid Lead-Halide Perovskites. *ACS Energy Lett.* **2019**, *4*, 17−25.

(125) Guo, R.; Zhao, G.; Wang, S. The Hot Carrier Dynamics of Graphitic Carbon Nitride/Molybdenum Disulfide Heterojunctions. *J. Phys. D: Appl. Phys.* **2019**, *52*, 385107.

(126) Li, W.; Zhang, X.; Lu, G. Unraveling Photoexcitation Dynamics at "Dots-in-a-Perovskite" Heterojunctions from First-Principles. *J. Mater. Chem. A* **2019**, *7*, 18012−18019.

(127) Chaban, V. V.; Pal, S.; Prezhdo, O. V. Laser-Induced Explosion of Nitrated Carbon Nanotubes: Nonadiabatic and Reactive Molecular Dynamics Simulations. *J. Am. Chem. Soc.* **2016**, *138*, 15927−15934.

(128) Zhou, X.; Tokina, M. V.; Tomko, J. A.; Braun, J. L.; Hopkins, P. E.; Prezhdo, O. V. Thin Ti Adhesion Layer Breaks Bottleneck to Hot Hole Relaxation in Au Films. *J. Chem. Phys.* **2019**, *150*, 184701.

(129) Wiebeler, C.; Plasser, F.; Hedley, G. J.; Ruseckas, A.; Samuel, I. D. W.; Schumacher, S. Ultrafast Electronic Energy Transfer in an Orthogonal Molecular Dyad. *J. Phys. Chem. Lett.* **2017**, *8*, 1086−1092.

(130) Zheng, Z.; Zheng, Q.; Zhao, J. Ultrafast Electron Transfer Dynamics in Lateral Transition-Metal Dichalcogenide Heterostructures. *Electron. Struct.* **2019**, *1*, No. 034001.

(131) Hyeon-Deuk, K.; Prezhdo, O. V. Time-Domain Ab Initio Study of Auger and Phonon-Assisted Auger Processes in a Semiconductor Quantum Dot. *Nano Lett.* **2011**, *11*, 1845−1850.

(132) Hyeon-Deuk, K.; Prezhdo, O. V. Multiple Exciton Generation and Recombination Dynamics in Small Si and CdSe Quantum Dots: An Ab Initio Time-Domain Study. *ACS Nano* **2012**, *6*, 1239−1250.

(133) Hyeon-Deuk, K.; Kobayashi, Y.; Tamai, N. Evidence of Phonon-Assisted Auger Recombination and Multiple Exciton Generation in Semiconductor Quantum Dots Revealed by Temperature-Dependent Phonon Dynamics. *J. Phys. Chem. Lett.* **2014**, *5*, 99−105.

(134) Akimov, A. V.; Prezhdo, O. V. Nonadiabatic Dynamics of Charge Transfer and Singlet Fission at the Pentacene/C_{60} Interface. *J. Am. Chem. Soc.* **2014**, *136*, 1599−1608.

(135) Sykora, M.; Mangolini, L.; Schaller, R. D.; Kortshagen, U.; Jurbergs, D.; Klimov, V. I. Size-Dependent Intrinsic Radiative Decay Rates of Silicon Nanocrystals at Large Confinement Energies. *Phys. Rev. Lett.* **2008**, *100*, No. 067401.

(136) Klimov, V. I.; McBranch, D. W.; Leatherdale, C. A.; Bawendi, M. G. Electron and Hole Relaxation Pathways in Semiconductor Quantum Dots. *Phys. Rev. B* **1999**, *60*, 13740−13749.

(137) Schaller, R. D.; Pietryga, J. M.; Goupalov, S. V.; Petruska, M. A.; Ivanov, S. A.; Klimov, V. I. Breaking the Phonon Bottleneck in Semiconductor Nanocrystals via Multiphonon Emission Induced by Intrinsic Nonadiabatic Interactions. *Phys. Rev. Lett.* **2005**, *95*, 196401.

(138) Sippel, P.; Albrecht, W.; Mitoraj, D.; Eichberger, R.; Hannappel, T.; Vanmaekelbergh, D. Two-Photon Photoemission Study of Competing Auger and Surface-Mediated Relaxation of Hot Electrons in CdSe Quantum Dot Solids. *Nano Lett.* **2013**, *13*, 1655−1661.

(139) Li, W.; Zhou, L.; Prezhdo, O. V.; Akimov, A. V. Spin−Orbit Interactions Greatly Accelerate Nonradiative Dynamics in Lead Halide Perovskites. *ACS Energy Lett.* **2018**, *3*, 2159−2166.

(140) Chen, L.; Bao, H.; Tan, T.; Prezhdo, O. V.; Ruan, X. Shape and Temperature Dependence of Hot Carrier Relaxation Dynamics in Spherical and Elongated CdSe Quantum Dots. *J. Phys. Chem. C* **2011**, *115*, 11400−11406.

(141) Kilina, S.; Velizhanin, K. A.; Ivanov, S.; Prezhdo, O. V.; Tretiak, S. Surface Ligands Increase Photoexcitation Relaxation Rates in CdSe Quantum Dots. *ACS Nano* **2012**, *6*, 6515−6524.

(142) Kilina, S. V.; Kilin, D. S.; Prezhdo, O. V. Breaking the Phonon Bottleneck in PbSe and CdSe Quantum Dots: Time-Domain Density Functional Theory of Charge Carrier Relaxation. *ACS Nano* **2009**, *3*, 93−99.

(143) Akimov, A. V.; Smith, B.; Shakiba, M.; Sato, K.; Temen, S.; Li, W.; Sun, X.; Chan, M. *Quantum-Dynamics-Hub/Libra-Code: Hotfix for the TD-DFT/NAMD with Libra (Version 4.9.1)*; Zenodo: 2020, DOI: 10.5281/Zenodo.4162542.

(144) Shakiba, M.; Smith, B.; Akimov, A. V. *AkimovLab/Project_Libra_CP2K: Data Files for Libra + CP2K Project (Version v1.0.3)*; Zenodo: 2021 , DOI: 10.5281/Zenodo.4161954.